Modelling Dusty Planetary Disks Using Secular Perturbation Theory

by

Christopher Claudio Capobianco

A Thesis Submitted to
Saint Mary's University, Halifax, Nova Scotia
in Partial Fullfilment of the Requirements for
the Degree of Masters of Science in Astronomy

October 2006, Halifax, Nova Scotia

Supervisor: Dr. Joseph M. Hahn,
Saint Mary's University

Examining Committee:
Dr. David A. Clarke,
Saint Mary's University
Dr. George Mitchell,
Saint Mary's University

Your file Votre référence
ISBN: 978-0-494-23851-6
Our file Notre référence
ISBN: 978-0-494-23851-6

Abstract

Modelling Dusty Planetary Disks

Using Secular Perturbation Theory

By Christopher Capobianco

Optical coronagraphic imaging of the circumstellar dust disk around β Pictoris reveals that the inner portion of the disk is warped, and this warp is typically attributed to the presence of a planetary system. Mouillet *et al.* (1997b) argue the warp is the result of a single planet on an inclined orbit, but the warp in their models are an artifact of their unphysical initial conditions. Using a more realistic set of initial conditions, at least *two* planets on mutually inclined orbits are required to produce the observed warp. The goal of this research is to find the two-planet configuration that best describes the warp in β Pictoris, using the more realistic set of initial conditions. This is accomplished via a parameter survey, where it is found that a $\sim 7M_J$ planet at 35 AU and a $\sim 3M_J$ planet at 131 AU, both on nearly circular orbits and inclined $\sim 2°$ to the disk mid-plane are able to accurately reproduce the observed warp in the β Pictoris disk.

Date: October, 2006

Acknowledgements

I would like to thank my supervisor Dr. Joeseph Hahn; this research would not have been possible if were not for all his help and support. I would also like to thank Dr. Sara Heap for graciously sharing her *HST* data on β Pictoris with us, and Dr. Ian Short for permitting the use of his computers to perform our parameter searches.

To my family and friends, thank you for all the support that you have given me. Finally to Mina, thank you for all your love, understanding and patience.

Contents

List of Figures

List of Tables

Chapter 1

Introduction

With the detection of cool dust by the *Infrared Astronomical Satellite (IRAS)* (Aumann, 1985), β Pictoris has emerged as the archetype for resolved circumstellar dust-disks around young Main Sequence stars. It has since been the subject of intensive monitoring campaigns at multiple wavelengths (Pantin *et al.*, 1997; Wahhaj *et al.*, 2003; Weinberger *et al.*, 2003; Okamoto *et al.*, 2004; Telesco *et al.*, 2005), and modelled extensively (Artymowicz, 1988; Kalas & Jewitt, 1995; Mouillet *et al.*, 1997b; Lecavelier des Etangs, 2000; Augereau *et al.*, 2001; Novotny, 2003).

Coronagraphic[1] imaging of β Pictoris reveals an asymmetric, flared disk extending beyond 1,000 AU from the star viewed nearly edge-on (Smith & Terrile, 1984; Kalas & Jewitt, 1995; Mouillet *et al.*, 1997a). High resolution *Hubble Space Telescope (HST)* images show that the inner portion of the disk ($\sim$ 20–100 AU) is warped $\sim 4.6°$ with respect to the mid-plane of the outer disk (see Figure 1.1). It has been suggested that this warp is maintained by a massive planet in a similarly inclined orbit (Mouillet *et al.*, 1997b; Heap *et al.*, 2000). Spatially resolved mid-infrared images of the inner disk show emission clumps within 100 AU, which appear in pairs centred on either side of β Pictoris. These clumps suggest the presence of dust in non-coplanar rings which could correspond to locations of mean-motion resonances with a suspected planetary system (Wahhaj *et al.*, 2003). However, only one of the clumps observed by Wahhaj *et al.* (2003) were detected in more recent high resolution mid-infrared observations by Telesco *et al.* (2005), and suggest that the remaining clumps in Wahhaj *et al.* (2003) are artifacts of noisy data.

[1] A coronagraph is a telescopic attachment designed specifically to obscure the light from a bright source, so that objects in the vicinity can be resolved without damaging the telescope's optics or saturating the detector.

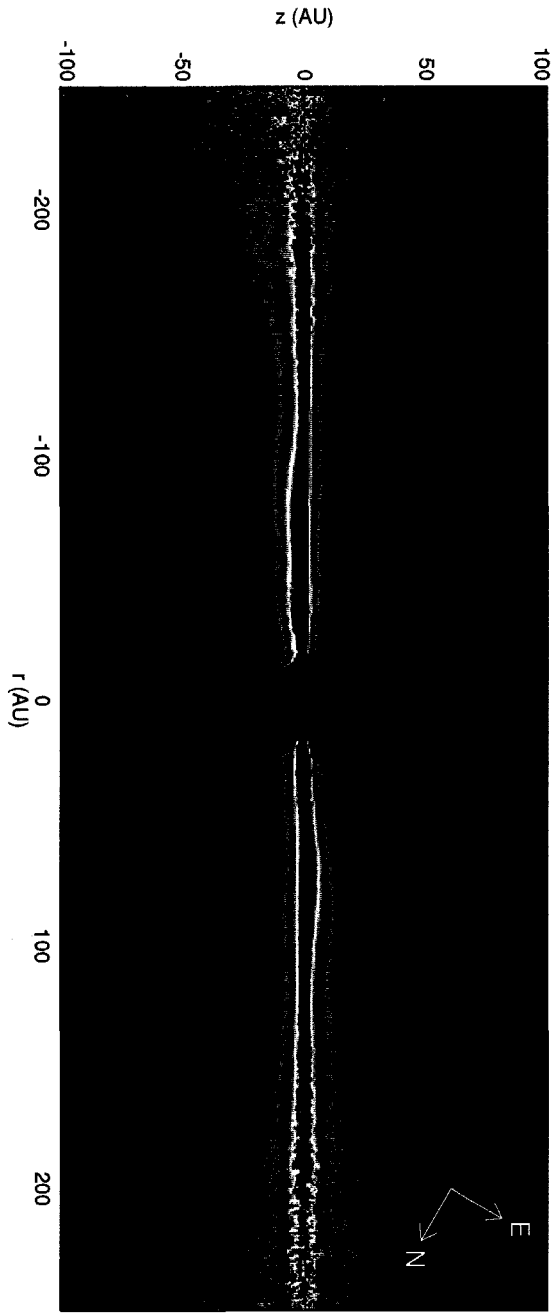

Figure 1.1: *HST* image of β Pictoris from Heap *et al.* (2000) with each row normalized to its peak value. This emphasizes the subtle $\sim 4.6°$ warp, which is indicated by the dotted line.

Warps in circumstellar disks have been observed in both real disks and theoretical models (Kalas & Jewitt, 1995; Kalas *et al.*, 2000; Heap *et al.*, 2000; Mouillet *et al.*, 1997b), and are generally attributed to the presence of planets. One of the more thorough analyses (Mouillet *et al.*, 1997b) argues that the warp observed in the β Pictoris disk is the result of a single planet, having an orbit that is inclined to the plane of the disk. In this scenario, gravitational torques due to this planet cause the dust grains' orbital planes to oscillate about the planet's orbital plane, with the dust grains nearer the planet oscillating faster than the more distant dust grains. This results in a kinematic warp in the disk that propagates radially outwards and away from the planet, which implies that such a warp will be relatively short–lived. However, warps can persist in more evolved systems; an example being the dust bands in the solar system. Furthermore, recent high-resolution *HST* images of β Pictoris have revealed that the β Pictoris disk has multiple warp features, which are not explained by the single-planet model of Mouillet *et al.* (1997b). We show that the kinematic warp occurring in the single-planet model of Mouillet *et al.* (1997b) is an artifact of unlikely initial conditions for the disk. When we adopt more plausible initial conditions, we demonstrate that at least *two* planets are required to account for the warp in the β Pictoris' disk.

This study is organized in the following manner. First we discuss some theoretical and observational background material in Chap. 2, then in Chap. 3 we discuss the relevant physical processes that take place in circumstellar disks. Chapter 4 describes in greater detail the physics of our model of a dusty planetary system, and Chap. 5 describes the algorithm we use to generate and fit our model to the *HST* image of β Pictoris. We report the results of the parameter searches in Chap. 6, and finally concluding remarks and possible future endeavours are given in Chap. 7.

Chapter 2

Background

Observational evidence suggests that gas and dust disks are ubiquitous around young protostars, which are a natural result of the star formation process (Beckwith, 1999). Over time, this material is subjected to numerous physical processes which results in the almost complete destruction of observable structure in the disk. In the following sections we briefly review the current picture of circumstellar disk formation, and its subsequent evolution.

2.1 Formation of Circumstellar Disks

According to the current paradigm of star formation, a young protostar forms via the gravitational fragmentation and collapse of a slowly rotating molecular cloud core (Shu *et al.*, 1987). The collapse of the cloud core leads to the formation of a central protostar, and since the collapse must also conserve angular momentum, some of the residual cloud material must go into orbit about the protostar in the form of a flattened disk. The remaining material in the envelope is removed either through accretion onto the protostar or the disk, or ejected via the protostar's radiation pressure or stellar winds.

There are three different types of circumstellar disks:

1. **Gas-rich disks** – Observed around young T Tauri stars (*e.g.* the Solar Nebula, the gas and dust from which the Solar System formed).

2. **Planetesimal disks** – The rocky or ice-rich solid bodies that are thought to coagulate in a young circumstellar disk. Planetesimals are the roughly $\sim$ 1 km asteroids or comets that are the progenitors of planets.

3. **Dust disks** – Circumstellar dust that is probably generated by collisions among unseen planetesimals.

The gas-rich disks tend to be quite massive *e.g.* $M_{gas} \sim 10^{-2} M_{\star}$ (where $M_{\star}$ is the mass of the central star), but they tend to last only a few Myrs as inferred from the lifetime of disks around young T Tauri stars (Strom *et al.*, 1993). Though gas-rich disks are predominately composed of hydrogen and helium gas from the protostellar nebula, they also contain small amounts of other gases *e.g.* CO, CS, HCO^+, NH_3, N_2H^+, *etc.* (Roberge *et al.*, 2000; Walmsley *et al.*, 2004) and dust (*e.g.* $M_{dust} \sim 10^{-2} M_{gas}$). The gas content of the disk is removed within a few Myrs after the formation of the protostar by one of several different disk dispersal mechanisms: accretion onto the central star, wind stripping, and photoevaporation (Hollenbach *et al.*, 2000), leaving behind a planetesimal debris disk. While accretion onto the central star and wind stripping are important removal mechanisms, photoevaporation is the dominant disk dispersal mechanism. Subsequent collisions between unseen planetesimals will generate large amounts of small dust particles, which will give rise to a circumstellar dust disk.

2.2 Formation of Planetesimals

There are two distinct planetesimal formation schemes: gravitational instability (Goldreich & Ward, 1973) and collisional accretion (Weidenschilling, 1980), though there is still no consensus which process actually forms planetesimals. Gravitational instability operates when the velocity dispersion of the dust grains become too low, and the planetesimal disks becomes gravitationally unstable to collapse, analogous to the Jean's instability. On the other hand, the collisional accretion model assumes that dust grains collide and stick together to form larger particles. In both scenarios, these larger particles will eventually lead to the formation of large planet-sized bodies (Alibert *et al.*, 2005). Throughout this study, we will concentrate on the collisional accretion mechanism to describe planetesimal formation. In dust-dust collisions, there are two possible outcomes: accretion

(the process of accumulation of dust into larger particles) or comminution (the pulverization of dust into smaller particles). The smallest of these particles will be blown away by radiation and stellar winds, while the larger particles will either accrete smaller particle or end up being pulverized into smaller dust particles through subsequent collisions.

While the gaseous component of the disk is still present, the solid particles will be affected by an aerodynamic gas drag. Due to the radial pressure gradient of the gas in the circumstellar disk which competes with the protostar's gravity, the gas will orbit at velocities that are slightly sub-Keplerian. As a consequence, the dust grains that orbit at Keplerian velocities feel a 'head-wind' which extracts angular momentum from their orbit and will cause them to spiral inwards. This acceleration is proportional to a grain's cross-sectional area per unit mass *i.e.* area/mass $\propto 1/s$ where s is the radius of the dust grain, so smaller particles will spiral in faster. As a result of this inward orbital decay, the frequency of collisions between particles will increase. This aerodynamic gas drag also causes grains to settle to the disk's mid-plane, since the vertical component of the drag force tends to damp out a dust grain's vertical motions and its orbital inclinations. As the density of solids in the mid-plane increases, the process of growth by collisions also increases. The process is enhanced as the particles get larger since they present a larger cross-sectional area, but they become less affected by gas drag. Bodies larger than $\sim$ 1 km, which are generally referred to as planetesimals, are largely immune to the effects of gas drag. It is from this distribution of planetesimals that planets then grow via collisional accretion.

In contrast to gaseous disks, the planetesimal debris is thought to have a mass of order $\sim 100 M_{\oplus}$ (where $M_{\oplus}$ is the mass of the Earth); this is simply the mass needed to form the solid cores of our own four giant planets (Hayashi, 1981). These debris disks probably persist much longer than gas disks, for perhaps $\sim$ 10–100 Myrs, but are typically not detected due to their low optical depth. These debris disks can also co-exist with a planetary system, like the asteroid belt at $\sim$ 3 AU and the Kuiper belt at $\sim$ 40 AU, which are remnants of the Solar System's original planetesimal disk. A circumstellar dust disk is thus suspected to be a product of collisions that occur in an unseen

circumstellar planetesimal disk. As a result of this evolutionary sequence, we typically find gaseous disks around very young stars *e.g.* $t_{age} < 10$ Myrs (Beckwith, 1999), and debris disks around older systems.

2.3 Previous Observations of β Pictoris

β Pictoris is one of the best-known examples of young Main Sequence stars with a resolved circumstellar dust-disk. It has been the subject of intensive studies ever since the discovery of infrared emissions from cool dust grains by *IRAS* (Aumann, 1985). In the following sections, the fundamental stellar parameters adopted for this study are summarized, and the previous observations and models of the β Pictoris dust-disk are briefly reviewed.

2.3.1 Stellar Parameters for β Pictoris

Based on the data collected by the *Hipparcos Satellite*, Crifo *et al.* (1997) was able to determine several of the stellar parameters (*e.g.* mass, distance and luminosity) for β Pictoris. More recently, Di Folco *et al.* (2004) determined an independent estimate of β Pictoris' radius using interferometric measurements from the *Very Large Telescope Interferometer (VLTI)*, while the age of β Pictoris was estimated by a comparison of β Pictoris' location in the *Hertzsprung-Russell Diagram* with theoretical stellar evolutionary models by Barrado y Navascués *et al.* (1999). The stellar parameters for β Pictoris' adopted for this study are summarized in Table 2.1.

2.3.2 The Gas Content Of β Pictoris' Circumstellar Disk

Most young main sequence stars show the presence of massive gaseous disks, yet, despite β Pictoris' relative youth, the amount of gas is very poorly constrained, typically below detection limits. The only strong detection of emission from a gaseous component has been the Na I doublet lines at 5990Å and 5996Å, whose signal is observed from $\sim$ 30 AU out to $\sim$ 140 AU (Olofsson *et al.*, 2001).

Table 2.1: Adopted Stellar Parameters for β Pictoris

Parameter	Value	Reference
Spectral Type	A5V	Hoffleit & Warren (1994)
Effective Temperature (T_{eff})	8200 ± 150 K	Lanz *et al.* (1995)
Stellar Mass ($M_\star$)	$1.75 \pm 0.10\ M_\odot$	Crifo *et al.* (1997)
Stellar Radius ($R_\star$)	$1.759 \pm 0.241\ R_\odot$	Di Folco *et al.* (2004)
Stellar Luminosity ($L_\star$)	$8.91 \pm 1.03\ L_\odot$	Crifo *et al.* (1997)
Distance (d)	19.28 ± 0.19 pc	Crifo *et al.* (1997)
Age (t_{age})	20 ± 10 Myrs	Barrado y Navascués *et al.* (1999)

Gas has also been detected through absorption lines of several ionized species: Ca II, Fe II, Mg II, Mn II and Al II, and to a lesser extent Na I and Fe I (Vidal-Madjar *et al.*, 1986; Lagrange-Henri *et al.*, 1998), but only in small quantities. Thébault & Augereau (2005) were able to show that the number density of hydrogen gas could not exceed $n_H \simeq 10^4$ cm^{-3} at 117 AU based on β Pictoris' scattered-light profile. The main result of their simulations is that high density gas disks always lead to dust distributions whose scattered-light profiles are strongly incompatible with the observations in the outer regions of the disk (*i.e.* $r \gtrsim 150$ AU), while in the inner regions of the disk (*i.e.* $r \lesssim 150$ AU) the scattered-light profile is insensitive to the effect of gas drag on the dust grains. Assuming the gas density profile of Brandeker *et al.* (2004), Thébault & Augereau (2005) are able to rule out gas disks with a total mass above $\sim 0.4 M_\oplus$.

β Pictoris' diminutive gaseous disk also exhibits an interesting peculiarity, it has three types of absorption line features: a stable component; a slowly varying component; and a rapidly varying component. Since the detection of Ca II absorption lines are seen in all observations at the same radial velocity as β Pictoris at 20 km/s, it is referred to as the stable gas component. The slowly varying component is usually found red-shifted 10–30 km/s with respect to the star, while the

rapidly varying component is found red-shifted 300–400 km/s but only detected in ionized species. The almost complete absence of complementary blue-shifted lines points to a mechanism that will preferentially direct the absorbing material away from us along our line of sight. These features might be explained by a planet that perturbs icy cometary material into star-grazing orbits; this is known as the Falling Evaporating Body (FEB) scenario (Beust *et al.*, 1990). The presence of ionized gas at large red-shifted velocities can be explained by the evaporation of the grains shed by the FEBs as they approach the star. A separate model by Levison *et al.* (1994) has suggested that secular planetary perturbations are another way of tossing planetesimals preferentially along a certain direction, so that an observer will usually see red-shifted events. However, there are discrepancies with both models so this phenomenon remains unexplained.

2.3.3 Dust Properties

The detection of infrared excess around nearby stars by *IRAS* created an rush of interest in stars like β Pictoris. The infrared excess is thought to be due to cool circumstellar dust grains absorbing photons from the central star and re-radiating at thermal infrared wavelengths (*i.e.* $\lambda \sim$20–100 μm). In β Pictoris this infrared excess is usually modelled as a blackbody with $T_{dust} \sim 85$ K at $r \sim 45$ AU, and from the *IRAS* measurements β Pictoris appeared to have a relatively substantial disk.

Zuckerman *et al.* (1993) was able to estimate the dust mass using sub-millimetre data. The disk's thermal emission is optically thin at sub-millimetre wavelengths, which allowed Zuckerman *et al.* (1993) to infer a total dust mass of $\sim 0.17 M_{\oplus}$ from his observations at 850 μm, assuming dust grains sizes of $s \sim 300$ μm. More recently, Dent *et al.* (2000) further refined this estimate by combining flux measurements from the mid-infrared to millimetre wavelengths, reducing the total dust mass to $\sim 0.04 M_{\oplus}$.

The detection of the 10 μm silicate emission feature by Telesco & Knacke (1991) also indicated that the dust in β Pictoris' circumstellar disk is similar to the material found in the solar system. Knacke *et al.* (1993) reports that the silicate features of β Pictoris are notably similar to those of

comets Halley, Bradfield 1987s and Levy 1990 XX. Subsequently, Li & Greenberg (1998) was able to model successfully the disk's continuum emission from the near-infrared to millimetre wavelengths, including the 10 μm silicate emission feature. Li & Greenberg assumed that the dust is continually replenished by comets orbiting in the vicinity of β Pictoris (*i.e.* 1 AU $\lesssim r \lesssim$ 40 AU).

Optical Colours and Dust Sizes

At optical wavelengths, the appearance of a circumstellar dust-disk will depend on the size of the dominant dust grain population, as well as the chemical composition of the dust grains. In a circumstellar dust-disk comprising predominately dust grains with $s \gg 1$ μm, the appearance of the disk will be optically neutral in colour. This is due to dust grains whose size is much larger than optical photons (*e.g.* $s \gg \lambda$), which are efficient scatterers of such photons. This condition is the basis of previous assertions that the reported neutral colours of β Pictoris' disk (see Figure 2.1) reflect a minimum grain size of several microns (Paresce & Burrows, 1987; Lecavelier des Etangs *et al.*, 1993).

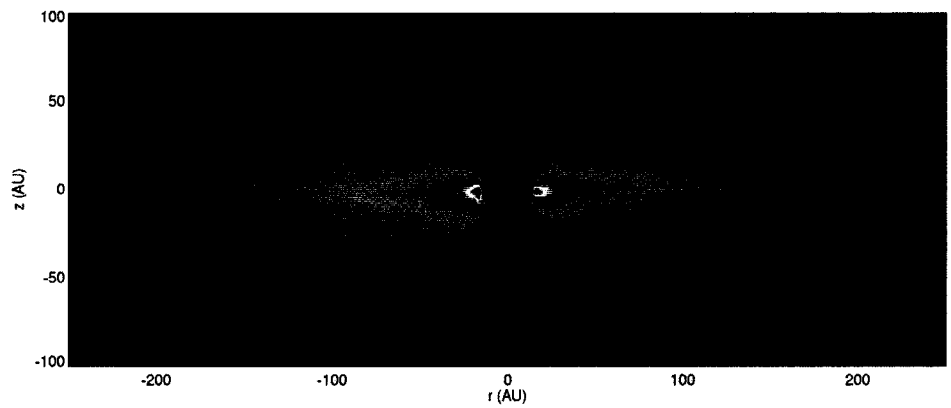

Figure 2.1: *HST* image of β Pictoris from Heap *et al.* (2000) on a linear intensity scale. The image was collected without any filters, so it represents the appearance of β Pictoris from 2,000Å to 10,000Å. The V-shaped gaps in the image are artifacts of the imperfect subtraction of the central stellar component.

Recent observations from the *Advance Camera for Surveys (ACS)* on *HST* by Golimowski *et al.* (2006) show that the optical colours of the disk are neutral within ~110 AU of the star, but redden considerably between 125 to 200 AU. This may reflect an increase in the minimum dust grain size with distance from $\sim$ 0.1 μm to perhaps $\sim$ 2 μm at 250 AU. The colour gradient appears to level off again from ~200 to 250 AU, but the relatively large uncertainties this far from the star make it difficult to say anything meaningful.

Constraints on the sizes of the dust grains observed in scattered-light have been based upon multi-band (*BVRI*) imaging studies of the disk in both unpolarized (Paresce & Burrows, 1987; Lecavelier des Etangs *et al.*, 1993) and polarized (Gledhill *et al.*, 1991; Wolstencroft *et al.*, 1995) light. The polarized images indicate that the disk is colourless (within 20–30% uncertainties) at distances 100–300 AU from β Pictoris. Attempts to reconcile the neutral colours of the disk with the 10–25% polarization of scattered-light from the disk have been problematic. Krivova *et al.* (2000) found that, although the polarization alone is best fitted with a grain size distribution with a lower limit of a few microns, the observed neutral colours can only be replicated by including a small amount of submicron-sized grains. Moreover, because small grains likely dominate the size distribution of grains in the disk (Dohnanyi, 1969; Li & Greenberg, 1998), they more strongly influence the overall colour of the disk than larger grains. Models of the spectral energy distribution for β Pictoris find that the typical dust grain size is $s \simeq 10$ μm, agreeing well with the available observational data (Krivov *et al.*, 2000).

2.3.4 Disk Morphology

The first direct image of β Pictoris was obtained by Smith & Terrile in 1984, which made use of a coronagraph to obscure the intense radiation from the central star. The image revealed a large ($r \sim 50'' \sim$ 1,000 AU), nearly edge-on disk with a peculiar surface brightness distribution. Further observations revealed the almost triangular shape of the disk's isophotes (see Figure 2.2), which shows a striking similarity to the zodiacal light distribution of the solar system. Also seen in these

images are a number of asymmetries in the surface brightness distribution. Using a coronagraph in the R band, Kalas & Jewitt (1995) obtained an image and identified five asymmetries: disk extent; brightness; disk width; the 'wing-tilt'; and the 'butterfly' asymmetry. The first three asymmetries refer to differences between the size, brightness and width of the northeast and southwest extensions of the disk. The northeast extension is both brighter and larger in extent than the southwest extension, while the southwest extension is wider than the northeast extension. The 'wing-tilt' asymmetry refers to the $\sim 1.3°$ misalignment between the mid-planes of the northeast and southwest extensions of the disk. The vertical brightness distribution in each extension also have different gradients above (*i.e.* $z > 0$) and below (*i.e.* $z < 0$) the disk mid-plane, and the 'butterfly' asymmetry refers to the steeper of these vertical brightness gradients in each extension are pointing in opposite directions. Specifically, the steeper vertical brightness gradient is above (*i.e.* $z > 0$) and below (*i.e.* $z < 0$) for the southwest and northeast extension, respectively.

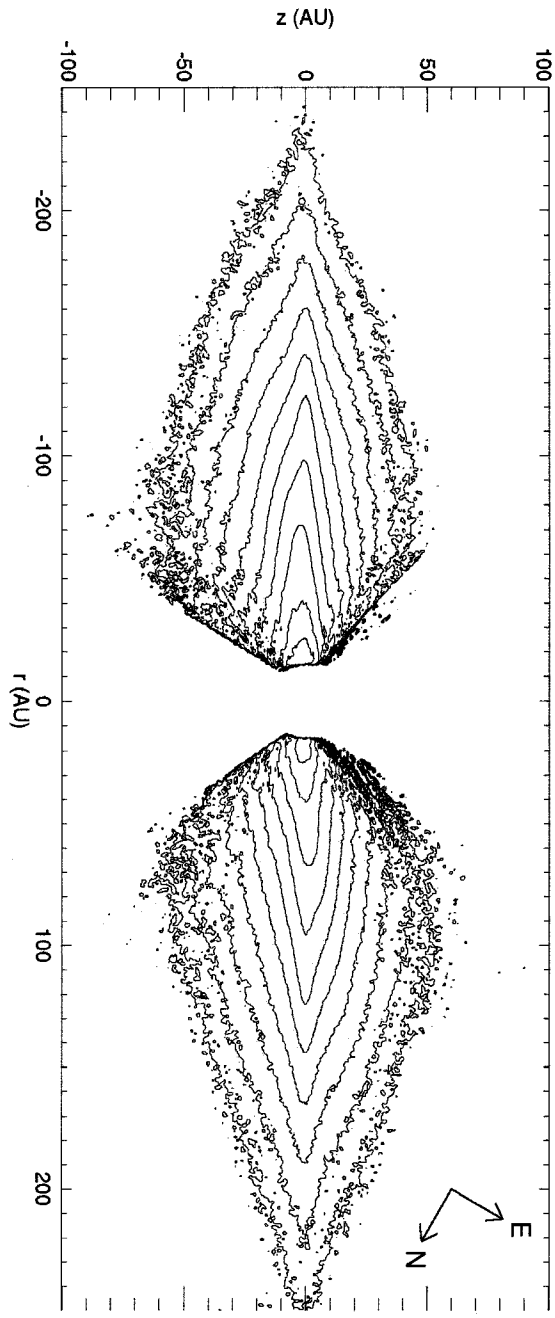

Figure 2.2: Isophotal contours of the *HST* image of β Pictoris from Heap *et al.* (2000) on a logarithmic intensity scale. The circular and X-shaped gaps in the data are due to the software mask (see §2.3.5) and diffraction spikes, respectively.

Recent high resolution *HST* observations by Heap *et al.* (2000) show that the inner portion (*i.e.* $r \lesssim 100$ AU) of the disk is warped $\sim 4.6°$ with respect to the mid-plane of the outer disk (see Figure 2.2). Heap *et al.* point out that the observations could be modelled using two mutually inclined disks, with the brighter and fainter components dubbed the main and inclined disk. The vertical thickness of both disk extensions appear nearly constant within $\sim$ 120 AU of β Pictoris, and increase almost linearly with distance beyond. The southwest extension also appears to widen more rapidly than the northeast extension beyond $\sim$ 160 AU, as noted by Kalas & Jewitt (1995).

More recent observations using the *Advance Camera for Surveys (ACS)* on *HST* by Golimowski *et al.* (2006) also note the brightness asymmetry above and below the mid-plane in the scattered-light image of β Pictoris, where the $z < 0$ portion is brighter than the $z > 0$ in Figure 2.2. Such a brightness asymmetry in optically thin disks is often attributed to the enhanced forward-scattering[1] by the dust, which implies that the nearer part of the β Pictoris disk is tipped slightly northwest from the line of sight to the star. This is consistent with the inclination determined by Kalas & Jewitt (1995) from single-scattering models of the surface brightness along the projected major axis of the disk.

The new results reported by Golimowski *et al.* (2006) have also cast some doubt on the possibility that β Pictoris harbours a young planetary system. Golimowski *et al.* present results collected using the *ACS* on *HST*, which has higher resolution than the *STIS* used to collect the data for this study. Their analysis of the deconvolved images claims that there are two distinct, mutually inclined disks which could *not* be explained by the presence of multiple planets. However, Golimowski *et al.* (2006) did not resolve any separation between these two purported disks, which implies that the observed disk could also be a single warped disk. So there are two favourable interpretations – two separate disks or a single warped disk – that are in agreement with the observations, and we are simply investigating the consequences of the second scenario.

[1]Forward-scattering is the tendency of a grain to scatter a photon preferentially in roughly the direction of its propagation, while back-scattering is the opposite.

Wahhaj *et al.* (2003) and Weinberger *et al.* (2003) later reported mid-infrared images of the disk that shows a distinct warp within 20 AU of the star (behind the occulting mask in Figure 2.2) tilted in the opposite direction from the more distant ($r \sim 100$ AU) inclined disk seen in Figure 2.2. Wahhaj *et al.* (2003) also note clumps of infrared emission in both disk extensions within 100 AU of β Pictoris that are arranged in pairs centred on either side on the star. They interpreted these clumps as a series of non-coplanar dust rings perhaps confined by gravitational interactions of the disk with a planetary system. However, these rings are not seen in optical observations by Heap *et al.* (2000) and Golimowski *et al.* (2006) or in mid-infrared observations by Telesco *et al.* (2005). High spatial resolution, mid-infrared spectra of the disk by Okamoto *et al.* (2004) show regions of concentrated emission from 0.1 and 2 μm silicate grains very close to the star at $r \sim 6.4$ AU and $r \lesssim 3.2$ AU, respectively. The presence of such concentrations of small grains in the face of strong radiation pressure suggests that the grains are created continuously by collisions between planetesimals.

Because β Pictoris' disk is viewed nearly edge-on, its surface brightness has traditionally been parametrized with one or more power-laws (*i.e.* $SB \propto r^{-\alpha}$) fitted along the mid-planes of its opposing extensions (Smith & Terrile, 1984; Artymowicz *et al.*, 1989; Lecavelier des Etangs *et al.*, 1993; Kalas & Jewitt, 1995; Mouillet *et al.*, 1997a; Heap *et al.*, 2000). Surface brightness profiles in scattered-light images of β Pictoris clearly indicate a prominent change in α at ~ 115 AU (Artymowicz *et al.*, 1990; Kalas & Jewitt, 1995; Heap *et al.*, 2000), as is illustrated in Figure 2.3. Typical values for α are 1.58 and 4.05 for the inner and outer portions of the disk [Table-3 from Golimowski *et al.* (2006)], respectively.

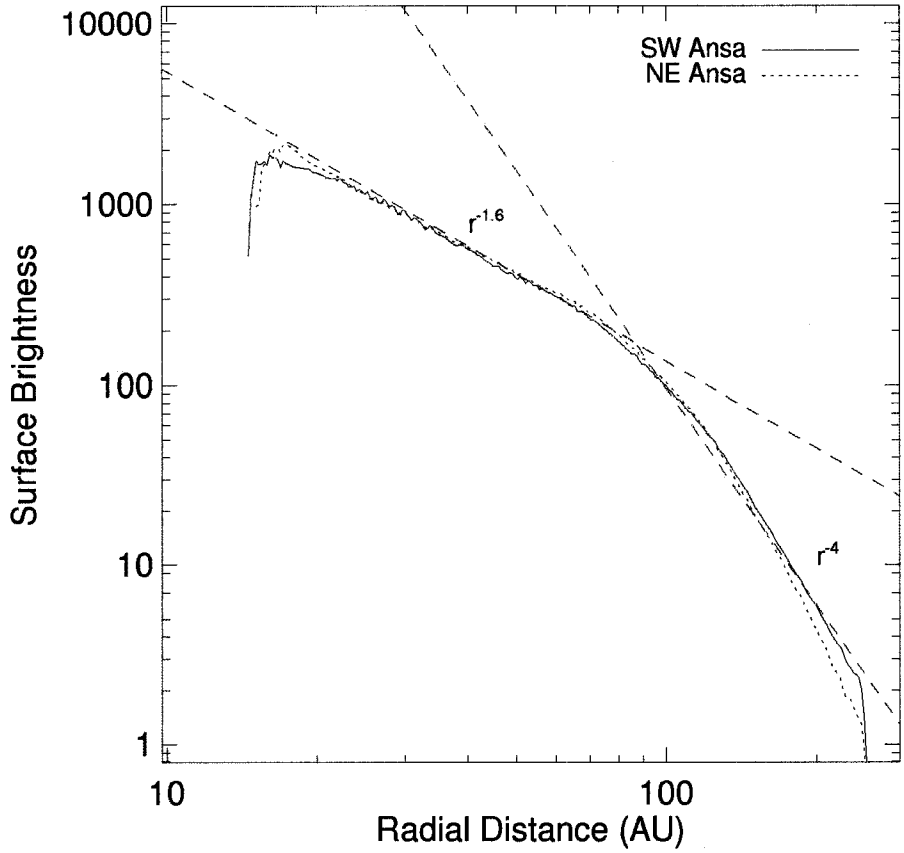

Figure 2.3: The radial surface brightness of β Pictoris' disk mid-plane, extracted from Figure 2.1, for the NE extension (dotted line) and the SW extension (solid line). The dashed lines are visual fits to the radial surface brightness for the inner and outer regions, with the radial dependence indicated adjacent to each line. The vertical scale is in arbitrary units.

2.3.5 The *HST* data

Throughout this study of the β Pictoris dust-disk, we make use of the surface brightness map provided by Sara Heap (see Figure 1.1 and Figures 2.1–2.2), which is also described in Heap *et al.* (2000). In the following, we summarize Heap's observations and her image processing.

The data were obtained coronagraphically with the *Space Telescope Imaging Spectrograph (STIS)* on the *Hubble Space Telescope (HST)*. The *STIS* employs an occulting mask and Lyot stop that work together to block out direct and scattered starlight. Due to its high angular resolution, $0.1'' \simeq 2.0$ AU at 19.28 pc for β Pictoris, it can accommodate small occulting masks allowing for examinations of the β Pictoris disk to within $0.5'' \simeq 10$ AU. However, to minimize the possible contaminates in determining the brightness distribution of the disk, Heap *et al.* applied a software mask to the diffraction spikes and the edges of the occulting mask. As a consequence of the software mask, imaging of the disk is limited to distances $r > 0.75'' \simeq 15$ AU. The *HST*'s stable and narrow point-spread function (PSF), whose full width at half maximum is $0.06''$ (in the V band) makes it possible to separate accurately the disk's light from the stellar contribution. The detector is a 1024×1024 pixel CCD, with each pixel subtending $0.0507''$.

For all the observations the aperture was left unfiltered, exposing the CCD to a wide band of light from 2,000Å to 10,000Å. Heap *et al.* collected two sets of observations, each using a different occulting mask and orientation to minimize contamination from known hot pixels. A series of eight 5.0 s exposures were recorded in one configuration, while two series of eight 3.0 s exposures were recorded for the other. Bias correction, flat-fielding and cosmic ray removal were performed for each set of eight exposures.

The separation of the stellar and disk contributions was achieved by acquiring occulted images of the star HD60753, whose optical properties are similar to β Pictoris, but with no known circumstellar structure. This image of HD60753 thus represents the PSF of a dust-free β Pictoris when observed behind an occulting mask. Heap *et al.* fitted the PSF to the β Pictoris observations in uncontaminated regions far from the disk plane, then the PSF is subtracted from the image of β Pictoris. Differencing these images, β Pictoris $-$ PSF, then provides a surface brightness map of the circumstellar disk that orbits β Pictoris (see Heap *et al.* (2000) for details). The final image was created by averaging each set of eight exposures (see Figure 2.1).

However, we were not provided the error map for the *HST* data, which is required for our planned

parameter surveys. In lieu of the actual error map, an estimate is generated based on the image itself. For each pixel in the image, the error is estimated by computing the standard deviation of a 3×3 box around that pixel. This estimate of the error map will be lower a limit on the real error map, since it does not take into account any instrumental or photometric uncertainties.

2.4 Previous Models of β Pictoris

The detection of several asymmetries from optical images of the circumstellar disk around β Pictoris (Kalas & Jewitt, 1995) touched off a flurry of models to describe these observed features. Some of these models have attempted to explain these features via a close stellar encounter, but the vast majority of these models are based on the existence of a planet in an inclined orbit. However, no single unified model has been able to explain all the observed asymmetries. In this section we review a few of these models and address their successes as well as their shortcomings.

2.4.1 Close Stellar Encounter Model

After subtracting a symmetric disk model from images of β Pictoris, Kalas *et al.* (2000) noticed several brightness enhancements $\sim$ 750 AU from the star in the northeast extension of the disk. Kalas *et al.* interpreted these brightness enhancements as a system of multiple rings seen edge-on. However, since they did not see the same brightness enhancements in the southwest extension, it was suggested that the rings were eccentric and only their apoapse[2] is visible.

In an effort to elucidate the nature of this ring system, numerical simulations of a close stellar encounter with a quiescent planetesimal disk were performed (Kalas *et al.*, 2000; Larwood & Kalas, 2001). The debris disk was modelled using 10^6 collisionless particles, initially on circular orbits. The perturbing star is assumed to have a mass of $\sim 0.3\ M_\star$ and would encounter the disk on a parabolic, non-coplanar trajectory. The encounter scatters particles outwards, launching a wake in

[2] Apoapse is the position of furthest distance to the central star along a given orbit. An eccentric particle ring tend to be densest at apoapse, since that is where a particle's orbital velocity is lowest.

the planetesimal disk that resembles an eccentric ring that can persists for at least 10^5 yrs, while the orbits of particles inside of $\sim$ 500 AU have become disorganized.

Multiple simulations were performed, and it was found that the best-fitting model occurred for a stellar encounter distance of $\sim$ 700 AU. At this distance, the probability of such an encounter is estimated to be $\sim 0.01\%$ in 10^6 years (Kalas *et al.*, 2000). Given that no suitable stellar candidate for such an encounter has been identified to date, this scenario is effectively ruled out.

2.4.2 Single Planet Models

The Falling Evaporating Body (FEB) model was proposed by Beust *et al.* (1990) to account for the transient red-shifted absorption events observed in β Pictoris. The absorption events come from ionized atomic species *e.g.* Ca II, Fe II and Mg II, which have large radial velocities with respect to the velocity of the β Pictoris system. Beust *et al.* (1990) proposed that a planet could perturb icy cometary material from the outer disk into star-grazing orbits, and as these comets approached the central star they would begin to evaporate, shedding gas and dust in the process. As the gas and dust fall towards the star, they would produce the red-shifted absorption lines at large velocities as observed in β Pictoris. Lagrange-Henri *et al.* (1988) estimated that to explain the frequency of these absorption events, $\sim$100 FEBs a year are required. However, Beust *et al.* (1990) does not provide any constraints on the mass, semi-major axis or eccentricity of the planet suspected to deliver the required number of FEBs. The main issue with this model is the particular viewing geometry, which is required to explain the almost complete absence of blue-shifted absorption events. Furthermore, the delivery mechanism requires the planet to perturb the FEBs into orbits that are preferentially parallel to our line of sight. Such requirements, therefore, make this model improbable.

Another model, championed by Mouillet *et al.* (1997b), attempts to explain high resolution scattered-light images from *HST* that show a slight warp of the inner portion of the disk, which is also the goal of this study. In their models, a quiescent planetesimal disk is subject to the gravitational perturbations from a single planet on an inclined orbit with respect to the disk. They accomplish

their simulations using smooth particle hydrodynamics, but the pressure and viscosity are ignored. The disk is modelled using 1.5×10^4 particles, and they follow the evolution of these particles for several thousand orbital periods of the perturbing planet. The planetesimals are initially placed on circular orbits in a disk with an aspect ratio $H/r = 0.1$, where H is the vertical thickness of the disk. The planetesimals were also distributed radially using a broken power-law to mimic the surface brightness distribution observed in β Pictoris. To compare their simulations with observations, Mouillet *et al.* generate synthetic surface brightness maps based on the location of the planetesimals at the end of the simulation.

The basic idea behind their models is that the observed warp is produced by a planet torquing the dust grains, which will cause their inclinations to oscillate about the planet's orbital plane. The frequency of these oscillations will decrease with distance from the planet, since more time is required for the planet's gravity to tilt the orbits of more distant dust grains. Thus the model of Mouillet *et al.* describes the warp as a kinematical wave propagating outwards as the dust grains are torqued by the planet. From their simple model, Mouillet *et al.* are able to derive the location of the warp as a function of time: $r \propto (ma^2 t)^{2/7}$, where m and a are the mass and semi-major axis of the planet. To place constraints on the mass and semi-major axis of the planet from the observed location of the warp, Mouillet *et al.* assume that the planet forms rapidly so that the propagation time of the warp is close to the age of the β Pictoris system. Combining their model with collected radial velocity measurements they are able to place the constraints on the mass of the planet ($10^{-5} \leq m/M_\star \leq 10^{-2}$) and the corresponding semi-major axis of the planet (20 AU $\leq a \leq$ 1 AU).

2.4.3 Model Limitations

In the previous sub-section, two separate single planet models were discussed, each attempting to explain a different observed phenomenon in β Pictoris. In the FEB model of Beust *et al.* (1990), we noted that the specific viewing geometry requirement was problematic. Now we address the

issues in the models of Mouillet *et al.* (1997b), which are used to explain the observed warp in the β Pictoris disk.

First, it should be noted that the progenitors of the dust grains (*e.g.* the unseen planetesimals) are expected to be distributed about the system's Laplace plane. The Laplace plane is the plane in which a particle's orbit will precess due to perturbations from massive bodies (Burns *et al.*, 1979b). Initially, planetesimals will not be distributed about the system's Laplace plane because they will possess nascent vertical and horizontal velocity dispersions. However, collisions between planetesimals will tend to drive their orbits towards the system's Laplace plane since these collisions will damp their nascent inclinations. The Laplace plane is actually a misnomer, since it is not a plane in general. The Laplace plane represents a surface determined by the orbits and masses of the planets, specifically through Eqns 4.11, which are discussed in greater detail in §4.3. In the case of a single planet, the Laplace plane is just the planet's orbital plane. However, for a system comprising $N \geq 2$ planets with mutual inclinations, the Laplace plane will be *warped.*

The main issue with the models of Mouillet *et al.* (1997b) are the initial conditions for the circumstellar disk. In their models, it is assumed the disk particles have an inclination $I \simeq 0.0°$ on average, and the planet's orbit is inclined to $I_f = 3.0°$. Under the assumption that these disk particles (*e.g.* planetesimals) are distributed about the system's Laplace plane (*i.e.* the planet's orbital plane), the inclination of the particles will contain two components: a proper component, and a forced component (*i.e.* $I \simeq I_p + I_f$). The forced component is gravitationally induced by the planet, and the proper component represents the nascent inclination in the absence of any perturbations. The initial conditions used in Mouillet *et al.* (1997b) are equivalent to having the proper inclination of each disk particle conspire to cancel the inclination of the planet (*i.e.* $I_p \simeq -I_f$), which is unphysical. While such artificial initial conditions are not impossible, they are highly improbable, so it is our claim that the initial conditions in Mouillet *et al.* (1997b) does not represent real circumstellar disks.

Now since we do expect the planetesimals and their dust grains in a disk to trace the system's Laplace plane, it will not be feasible to produce a warp with only a single planet. The minimum

requirement to produce the warp detected in the scattered-light image of β Pictoris, is at least *two* planets on non-coplanar orbits. While the models from Mouillet *et al.* (1997b) do reproduce the warp seen around ~80–100 AU in β Pictoris, this is just an artifact of their unrealistic initial conditions.

Chapter 3

Physical Processes in Circumstellar Disks

There are several physical processes that can occur in circumstellar disks; of these, only a few are relevant to dust grains in the β Pictoris disk. Specifically, the dynamics of dust grains will be affected by gravitational perturbations from planets, radiation forces from the central star, and dust–dust collisions. For each process there is an associated timescale based on the environmental conditions within the disk. A comparison of these various timescales will reveal the dominant process in the disk, where the process operating on the shortest timescale will have the greatest effect on the dynamics within the disk. This section briefly reviews each of these processes, and discusses their relative importance.

3.1 Gravity

The dominant influence in the circumstellar environment is the gravity of the central star. However, gravitational perturbations can also come from other massive bodies (*e.g.* planets) within the system. The timescale associated with the influence from the central star is simply the Keplerian orbital period which comes from Kepler's third law:

$$P_{orb} = 2\pi\sqrt{\frac{a^3}{G(M_\star + m)}} \tag{3.1}$$

where P_{orb} is the orbital period, a and m are the semi-major axis and mass of an orbiting body, $M_\star$ is the mass of the central star, and G is the gravitational constant. Alternatively, this can also be written as the mean orbital frequency

$$n = \frac{2\pi}{P_{orb}} = \sqrt{\frac{G(M_\star + m)}{a^3}} \tag{3.2}$$

We will discuss the role of gravity further in the next chapter.

3.2 Radiation Forces

All particles in a circumstellar disk interact with radiation from the central star. The magnitude of the radiation effects is proportional to a particle's cross-section per unit mass *i.e.* area/mass $\propto 1/s$ where s is the radius of the dust grain. For larger particles the central star's gravity will be the dominant force, while sufficiently small particles can be blown away by radiation pressure. The relative importance of radiation forces to the stellar gravity is governed by their ratio β (Burns *et al.*, 1979a):

$$\beta \equiv \frac{F_{rad}}{F_{grav}} = \frac{3L_{\star}Q_{PR}}{16\pi GM_{\star}\rho cs} \tag{3.3}$$

where ρ and s are the density and radius of the particle, $L_{\star}$ is the luminosity of the central star, and c is the speed of light. Q_{PR} is the radiation pressure efficiency factor which takes into account both the absorption and scattering efficiencies of the particle [*i.e.* $Q_{PR} = Q_{abs} + (1-g)Q_{sca}$, where g is the scattering asymmetry parameter]. Q_{PR} is typically a complicated function of size, structure and composition of the particle as well as the wavelength of the incident radiation. For a typical silicate grain of size $s \sim 10$ μm at optical wavelengths (*i.e.* $\lambda \sim 0.6$ μm), Q_{PR} is on the order unity (Wolf & Voshchinnikov, 2004).

The radiation force has two distinct components, known as radiation pressure and Poynting-Robertson drag. Radiation pressure is the name given to the radial component of the radiation force. Since each photon carries momentum, this momentum can be transferred to a particle as it absorbs or scatters stellar photons, and the rate at which this momentum transfer occurs per cross-sectional area of a particle constitutes a pressure. Since radiation pressure is directly radially outward and varies as r^{-2}, it therefore counters the effect of gravity. Thus a particle behaves as if it were orbiting a star with an effective mass that is reduced by a factor $1-\beta$. In β Pictoris with $M_{\star} = 1.75M_{\odot}$ and $L_{\star} = 8.91L_{\odot}$, for a typical dust grain size of $s \sim 10$ μm and dust grain density

of $\rho \sim 2.0$ g/cm^3 gives $\beta \sim 0.15$, where we have assumed $Q_{PR} = 1$. Since β is inversely proportional to the radius of the particle, smaller particles will have larger β values, and those with $\beta > 0.5$ are quickly ejected from the system on hyperbolic orbits. Thus the relevant timescale for radiation pressure acting on small grains having $\beta > 0.5$ will be on the order of an orbital period.

The Poynting-Robertson force results from the component of the radiation force that is tangential to the particle's orbit. Since this force is velocity dependent, it acts as a dynamic drag. We can understand this effect if we make an analogy with driving in the rain on a windless day. While the vehicle (*i.e.* the dust grain) is at rest, the raindrops (*i.e.* photons) will simply fall vertically. However, once the vehicle is in motion, the same raindrops strike the vehicle from the forward direction when viewed from the vehicle's frame of reference. This also transfers momentum from the vehicle to the rain, so the rain exerts a slight drag on the vehicle. It is also worth noting that this same phenomenon results in the aberration of starlight, which is the angular displacement of a star due to the Earth's orbital motion and the finite speed of light. Thus from the frame of reference of a dust grain, the Poynting-Robertson force will appear to oppose the dust grain's motion. As a result, these interactions will remove angular momentum from the dust grain's orbit and will cause the dust grain to spiral towards the central star on a timescale that is inversely proportional to β (Burns *et al.*, 1979a):

$$t_{PR}(r) = \frac{P_{orb}(r)c}{8\pi\beta nr} \tag{3.4}$$

where $P_{orb}(r)$ is the Keplerian orbital period at r. Using typical values for $\beta \sim 0.15$, $r \sim 100$ AU and $P_{orb}(r) \sim 800$ yrs gives a Poynting-Robertson drag timescale of $t_{PR}(r)$ ~15 Myrs in β Pictoris.

3.3 Collisions

Collisions play an important role in circumstellar disks since they provide a mechanism for both the creation and destruction of dust particles. Theoretical models predict a very steep size distribution for particles that are in collisional equilibrium, where there are many more smaller particles than

larger particles. Thus, the disk's optical depth tends to be dominated by these smaller particles (Wyatt *et al.*, 1999). However, these smaller grains will also experience radiation effects (*e.g.* radiation pressure and Poynting-Robertson drag) that can quickly remove them from the system. Therefore if small particles are present in a circumstellar disk then there must be a source of dust, likely colliding planetesimals.

The collision timescale depends on the cross-sectional area of the particle, as well as the distribution of cross-sectional area from the particle population. However, as already mentioned, the predominance of smaller particles allows us to simplify by only considering a single particle size. The collisional timescale is

$$t_{coll}(r) = \frac{P_{orb}(r)}{2\tau(r)} \tag{3.5}$$

where $\tau(r)$ is the normal optical depth at the radial distance r from the central star [see Eqn (C.3) in Appendix C]. The normal optical depth represents the fraction of the disk that is occupied by dust particles. If $t_{coll}(r) \ll t_{PR}(r)$, then we can ignore Poynting-Robertson drag in our modelling since grains will be destroyed before drifting very far. This is a key assumption in our models, one that is supported by observations of the β Pictoris dust-disk (see Appendix C). Using the same typical values for $r \sim 100$ AU and $P_{orb}(r) \sim 800$ yrs, and $\tau(r) \sim 5 \times 10^{-3}$ from Artymowicz (1997) gives a collisional timescale of $t_{coll}(r) \sim 0.1$ Myrs in β Pictoris. Since $t_{coll}(r) \ll t_{PR}(r)$, this justifies our neglect of Poynting-Robertson drag.

3.4 Other Forces

The circumstellar environment is very complex, and there are many other forces that can affect the dynamics of dust particles. While these forces should not be ignored in general, we justify why we can safely neglect them in this study of the β Pictoris disk.

3.4.1 Gas Drag

For very young main sequence stars, massive gaseous disks are ubiquitous. In such systems, the effects of gas drag must be taken into consideration when describing the dynamics of dust grains. As discussed in §2.3.2, the current estimates place the mass of gas in β Pictoris at $\simeq 0.4 M_{\oplus}$, which is comparable to estimates of the dust mass (Dent *et al.*, 2000). Thébault & Augereau (2005) were able to show that for such small amounts of gas, the dynamics of dust inwards of ~150 AU are insensitive to gas drag. They also noted that while the effects of gas drag may still be important at larger distances (*e.g.* $r \gg 150$ AU), gas drag is negligible for the regions of interest in this study (*e.g.* $r < 150$ AU), and we shall ignore its effects.

3.4.2 Stellar Wind

The stellar wind is a flux of charged particles that escapes a star's atmosphere. The dust particles can interact with the stellar wind in two ways: directly through collisions and through a Lorentz force. The Lorentz force arises from the fact that the dust particles tend to be charged, and the stellar wind particles carry with them a magnetic field. The stellar wind is a result of coronal and chromospheric activity, and is typically associated with stars that have a deep convective envelope. However, A-type stars like β Pictoris do not possess deep convective envelopes. As a result, we do not expect that stellar winds will be important in the case of β Pictoris.

3.5 Summary

From our analysis of the circumstellar environment, we recognize that a number of the physical processes in circumstellar disks outlined in the chapter can be safely ignored. Though we wish to stress that our analysis is not comprehensive, and should not be applied blindly to other systems. We note that from the subset of relevant physical processes, all the forces (except gravity) have a preferred particle scale. For the smallest particles (*e.g.* $s < 1$ μm), radiation pressure is the

most dominant process and will quickly remove them from the system. Intermediate size particles (*e.g.* $s \sim 1$ μm) are removed by spiralling towards the central star through Poynting-Robertson drag, over a timescale of ~15 Myrs in β Pictoris. Larger particles (*e.g.* $s \gtrsim 10$ μm) will get collisionally destroyed over a timescale of ~0.1 Myrs in β Pictoris, while the largest particles (*i.e.* the planetesimals) will only be affected by gravity.

All these processes (except gravity, again) tend to deplete the circumstellar disk of dust grains rapidly on timescales much shorter than β Pictoris' ~20 Myrs lifetime, however observations of its circumstellar disk reveals the presence of dust despite the age of β Pictoris. This implies that the dust grain populations are being replenished (Li & Greenberg, 1998), and the main source of such dust grains is likely collisions among unseen planetesimals. As outlined earlier, the aim of this chapter is to shed some light on the relevant physical processes by comparing their corresponding timescales. From estimates of the normal optical depth $\tau(r) \sim 5 \times 10^{-3}$ at $r \sim 100$ AU (Artymowicz, 1997), we were able to demonstrate that the β Pictoris circumstellar disk is collisionally dominated [*i.e.* $t_{coll}(r) \ll t_{PR}(r)$]. This is convenient, since this allows us to model the orbits of the dust grains as if they were static (*i.e.* they don't drift radially due to Poynting-Robertson drag or radiation pressure), which makes the modelling effort described in Chapter 4 considerably easier.

Chapter 4

Secular Perturbation Theory

In the previous chapter we discussed the relevant physical processes in circumstellar disks, and it was shown that β Pictoris' circumstellar disk is in the collisionally dominated regime (*i.e.* $t_{coll} \ll t_{PR}$). However, until now we have not discussed the effects of gravity in circumstellar disks. There are three distinct ways that a planet can gravitationally perturb a dust grain, though not all are relevant:

1. **Gravitational Scattering** – Repeated scattering usually results in the dust grain either getting ejected from the system, or suffering a collision with a planet or the central star. This scattering happens on a short timescale (*i.e.* the orbital period), thus dust grains that are apt to get scattered are quickly removed from the system and can be ignored in our modelling effort.

2. **Resonant Perturbations** – Each planet has an infinite suite of such mean-motion resonances, which are sites where the dust to planet orbital periods are in ratios of whole numbers, such as the 2:1, 3:2, 4:3, *etc.*[1] However, the fractional width of a mean-motion resonance is $\Delta a/a \sim 1.6\mu^{2/3}$ where μ is the planet to star mass ratio (Wisdom, 1980). Thus the fractional resonance width for a Jupiter-mass planet having $\mu = 10^{-3}$ is only $\Delta a/a \sim 0.01$. Of course, there are an infinite number of such resonances, but most of those lay very near the planet's orbit, and dust orbits at those resonances are also apt to get scattered and removed. Thus if mean-motion resonances play any role, only the outermost will be relevant (*e.g.* the 2:1, 3:2 and maybe the 4:3 mean-motion resonances), and they will only perturb a tiny portion ($\sim$ a few %) of the dust disk due to their tiny width. In most cases, these resonances will have little or no influence on

[1] In the language of galactic dynamics these are called Lindblad resonances, *i.e.* the $m = 1$ Lindblad resonance is the 2:1 mean-motion resonance; the $m = 2$ Lindblad resonance is the 3:2 mean-motion resonance, *etc.*

the observed appearance of a circumstellar disk, and we are justified in ignoring them here.

3. **Secular Perturbations** – Nonetheless, dust grains orbiting everywhere else (*e.g.* in between and beyond the mean-motion resonances) will still be perturbed by the planets secular perturbations. Loosely speaking, a planet's secular perturbations are the parts of a planet's gravitational potential that, when Fourier decomposed, do not have any explicit time dependence; those forces correspond to planets that have had their masses smeared out about their orbital ellipse. So when studying the secular evolution of a dusty planetary system, we are examining it in the time-averaged sense. It should also be noted that these secular perturbations do not alter the semi-major axis of planets or the dust grains (Brouwer & Clemence, 1961). The great advantage of considering the system's evolution due to secular perturbations is that the motion is completely analytic – one can readily compute the orbital elements of all the planets and dust grains at any instant in time, so one can rapidly compute the surface brightness of a perturbed dust disk.

In the following sections, we outline the modelling scheme using secular perturbation theory to calculate the disk's appearance, which is presumably disturbed by a system of embedded planets. This approach is, of course, valid only if the mean-motion resonances of those planets do not play a major role in determining the disk's structure. This appears to be the case for most perturbed dust-disks that have been observed to date: β Pictoris (Mouillet *et al.*, 1997a), HR4796A (Schneider *et al.*, 1999) and Fomalhaut (Kalas *et al.*, 2005). One notable exception to this rule is the dust ring at ϵ Eridani, whose lumpy appearance has been successfully modelled as dust trapped at a 3:2 mean-motion resonance with a Neptune-mass ($\mu = 10^{-4}$) planet (Quillen & Thorndike, 2002). However, all other perturbed dust-disks are either broadly eccentric or warped, which suggests that secular planetary perturbations are the major operative. In the following we describe in greater detail the secular perturbation theory we use to simulate a circumstellar dust-disk that is perturbed by a system of embedded planets.

4.1 The Secular Equations of Motion

Before we begin, we first need to define all the relevant orbital elements used in this study. The mean orbital distance between an object and the central star, a, is referred to as the semi-major axis of the orbital ellipse. The measure of how much the shape of the orbit deviates from a circle, e is referred to as the eccentricity. For circular orbits $e = 0$, while in general for elliptical orbits $0 < e < 1$. The angle between the orbital plane and the $\hat{x}$-$\hat{y}$ reference plane of Figure 4.1 is the inclination I. The angle between the positive $\hat{x}$-axis and the location where orbit 'ascends' through the reference plane, Ω, is referred to as the longitude of the ascending node. The angle between the ascending node and the the position of closest approach to the central star (pericentre), ω, is referred to as the argument of periapse. A more common angle used in celestial mechanics is $\varpi = \omega + \Omega$, which is the sum of *non-coplanar* angles and is referred to as the longitude of periapse (as measured from the positive $\hat{x}$-axis). See Figure 4.1 for an illustration of these quantities.

It is convenient to transform body j's orbital elements e_j, ϖ_j, I_j and Ω_j into vertical and horizontal components of eccentricity and inclination "vectors" whose Cartesian coordinates are $\vec{e}_j = (k_j, h_j)$ and $\vec{I}_j = (q_j, p_j)$. Their magnitudes are simply the body's eccentricity and inclination, and these vectors point in the direction of periapse and the ascending node, respectively. These vectors have Cartesian coordinates:

$$h_j = e_j \sin \varpi_j \qquad k_j = e_j \cos \varpi_j \tag{4.1a}$$

$$p_j = I_j \sin \Omega_j \qquad q_j = I_j \cos \Omega_j \tag{4.1b}$$

where p_j and q_j can be interpreted as projections of a grain's angular momentum vector $\vec{L}$ onto the equatorial plane (see Figure B.1). We also note that $\vec{e}_j$ is the the Laplace-Runge-Lenz vector from classical mechanics, and both $\vec{e}_j$ and $\vec{L}_j$ are conserved in the absence of any perturbations.

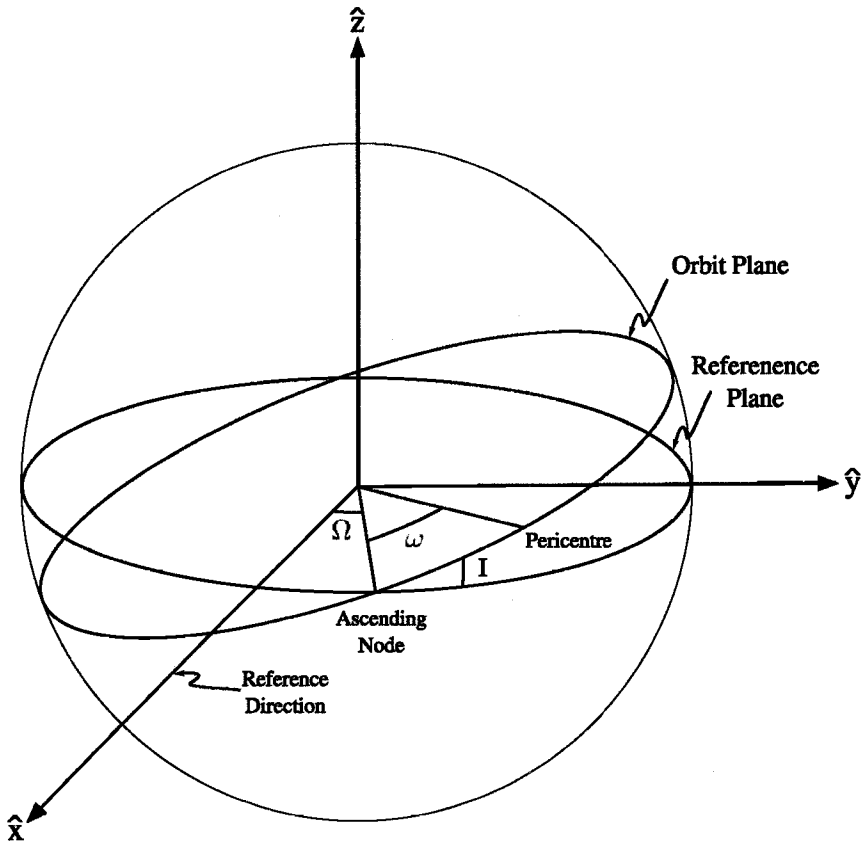

Figure 4.1: Orbital element definitions

4.2 The Secular Evolution of N Planets

Now that the quantities h_j, k_j, p_j and q_j have been defined, it just remains to obtain the secular equations of motion to describe their evolution. The secular equations of motion can be found in Murray & Dermott (1999), but for a derivation of the secular equations of motion for p_j and q_j from first principles, we refer the readers to Appendix B. At this point we will simply quote the general

N-body secular equations of motion for a body of mass m_j given by Eqns (B.9) and Eqns (B.11):

$$\dot{h}_j = A_{jj}k_j + \sum_{\substack{i=1 \\ i\neq j}}^{N} A_{ji}k_i \qquad \dot{k}_j = -A_{jj}h_j - \sum_{\substack{i=1 \\ i\neq j}}^{N} A_{ji}h_i \tag{4.2a}$$

$$\dot{p}_j = B_{jj}q_j + \sum_{\substack{j=1 \\ i\neq j}}^{N} B_{ji}q_i \qquad \dot{q}_j = -B_{jj}p_j - \sum_{\substack{i=1 \\ i\neq j}}^{N} B_{ji}p_i \tag{4.2b}$$

where

$$A_{ji} = -\frac{1}{4}\frac{m_i}{M_\star + m_j} n_j \alpha_{ji} b^{(2)}_{3/2}(\alpha_{ji}) \qquad A_{jj} = +n_j \frac{1}{4}\sum_{\substack{i=1 \\ i\neq j}}^{N} \frac{m_i}{M_\star + m_j} \alpha_{ji} b^{(1)}_{3/2}(\alpha_{ji}) \tag{4.3a}$$

$$B_{ji} = +\frac{1}{4}\frac{m_i}{M_\star + m_j} n_j \alpha_{ji} b^{(1)}_{3/2}(\alpha_{ji}) \qquad B_{jj} = -n_j \frac{1}{4}\sum_{\substack{i=1 \\ i\neq j}}^{N} \frac{m_i}{M_\star + m_j} \alpha_{ji} b^{(1)}_{3/2}(\alpha_{ji}) \tag{4.3b}$$

where n_j is the mean orbital frequency (mean motion) of planet j whose mass is m_j, $\alpha_{ji} \equiv a_i/a_j$ is the semi-major axis ratio between m_j and m_i, while $M_\star$ is the mass of the central star. The quantities $b^{(1)}_{3/2}(\alpha_{ji})$ and $b^{(2)}_{3/2}(\alpha_{ji})$ are the Laplace coefficients as defined in (A.14). The quantities A_{ji} and B_{ji} can be thought of as the constant elements of two $N \times N$ matrices $\mathbf{A}$ and $\mathbf{B}$ whose entries describe the magnitude of the mutual gravitational interactions that are exerted among the N planets (Murray & Dermott, 1999; Hahn, 2003).

Equations (4.2) form two sets of N-coupled linear differential equations with constant coefficients, and the solution for such a system can be formed from the eigenvalues and eigenvectors of the $\mathbf{A}$ and $\mathbf{B}$ matrices (Boyce & DiPrima, 1997):

$$h_j(t) = \sum_{i=1}^{N} e_{ji}\sin(g_i t + \beta_i) \qquad k_j(t) = \sum_{i=1}^{N} e_{ji}\cos(g_i t + \beta_i) \tag{4.4a}$$

$$p_j(t) = \sum_{i=1}^{N} I_{ji}\sin(f_i t + \gamma_i) \qquad q_j(t) = \sum_{i=1}^{N} I_{ji}\cos(f_i t + \gamma_i) \tag{4.4b}$$

where the frequencies g_i are the eigenvalues of $\mathbf{A}$, f_i are the eigenvalues of $\mathbf{B}$, while e_{ji} and I_{ji} are the elements of the N eigenvectors of $\mathbf{A}$ and $\mathbf{B}$. The phases β_i and γ_i, as well as the magnitude of the eigenvectors, are determined from the initial conditions using the prescription given in Murray & Dermott (1999). Also, we note that the solutions (4.4) are identical to that given in Murray & Dermott (1999), albeit derived using different methods.

4.3 The Secular Evolution of a Massless Dust Grain

Now that we can obtain the orbital elements foo each of the N planets as a function of time, we can study the motion of an additional body of negligible mass, moving under the influence of the central star and perturbed by these other massive bodies. The equations of motion for a massless particle are Eqns (4.2), and are also solved in Murray & Dermott (1999):

$$\dot{h} = Ak + \sum_{j=1}^{N} A_j k_j \qquad \dot{k} = -Ah - \sum_{j=1}^{N} A_j h_j \tag{4.5a}$$

$$\dot{p} = Bq + \sum_{j=1}^{N} B_j q_j \qquad \dot{q} = -Bp - \sum_{j=1}^{N} B_j p_j \tag{4.5b}$$

where the A and B coefficients are

$$A_j = -\frac{1}{4}\frac{m_j}{M_\star} n\alpha_j b_{3/2}^{(2)}(\alpha_j) \qquad A = +n\frac{1}{4}\sum_{j=1}^{N}\frac{m_j}{M_\star}\alpha_j b_{3/2}^{(1)}(\alpha_j) \tag{4.6a}$$

$$B_j = +\frac{1}{4}\frac{m_j}{M_\star} n\alpha_j b_{3/2}^{(1)}(\alpha_j) \qquad B = -n\frac{1}{4}\sum_{j=1}^{N}\frac{m_j}{M_\star}\alpha_j b_{3/2}^{(1)}(\alpha_j) \tag{4.6b}$$

where n is the mean motion of the massless particle and $\alpha_j \equiv a/a_j$ is the ratio of the semi-major axis of the massless particle to planet j. However, the quantities h_j, k_j, p_j and q_j are known functions of time, Eqns (4.4), and they describe the motions of the planets. Substituting Eqns (4.4) into Eqns (4.5) yields four coupled, first-order differential equations

$$\dot{h} = +Ak + \sum_{j=1}^{N} A_j \sum_{i=1}^{N} e_{ji}\cos(g_i t + \beta_i) \tag{4.7a}$$

$$\dot{k} = -Ah - \sum_{j=1}^{N} A_j \sum_{i=1}^{N} e_{ji}\sin(g_i t + \beta_i) \tag{4.7b}$$

$$\dot{p} = +Bq + \sum_{j=1}^{N} B_j \sum_{i=1}^{N} I_{ji}\cos(f_i t + \gamma_i) \tag{4.7c}$$

$$\dot{q} = -Bp - \sum_{j=1}^{N} B_j \sum_{i=1}^{N} I_{ji}\sin(f_i t + \gamma_i) \tag{4.7d}$$

If we take another time derivative of each equation and substitute back (4.7), then after a little

manipulation we get four second-order differential equations that are now uncoupled

$$\ddot{h} = -A^2 h - \sum_{i=1}^{N} \nu_i (A + g_i) \sin(g_i t + \beta_i) \tag{4.8a}$$

$$\ddot{k} = -A^2 k - \sum_{i=1}^{N} \nu_i (A + g_i) \cos(g_i t + \beta_i) \tag{4.8b}$$

$$\ddot{p} = -B^2 p - \sum_{i=1}^{N} \kappa_i (B + f_i) \sin(f_i t + \gamma_i) \tag{4.8c}$$

$$\ddot{q} = -B^2 q - \sum_{i=1}^{N} \kappa_i (B + f_i) \cos(f_i t + \gamma_i) \tag{4.8d}$$

where

$$\nu_i - \sum_{j=1}^{N} A_j e_{ji} \qquad\qquad \kappa_i - \sum_{j=1}^{N} B_j I_{ji} \tag{4.9}$$

Eqns (4.8) resemble the equations of motion for a forced simple harmonic oscillator, so the solutions to these differential equations are simply

$$h(t) = e_p \sin(At + \varpi_p) + h_f(t) \qquad k(t) = e_p \cos(At + \varpi_p) + k_f(t) \tag{4.10a}$$

$$p(t) = I_p \sin(Bt + \Omega_p) + p_f(t) \qquad q(t) = I_p \cos(Bt + \Omega_p) + q_f(t) \tag{4.10b}$$

where e_p, I_p, ϖ_p and Ω_p are constants determined from the initial conditions and

$$h_f(t) = -\sum_{i=1}^{N} \frac{\nu_i}{A - g_i} \sin(g_i t + \beta_i) \tag{4.11a}$$

$$k_f(t) = -\sum_{i=1}^{N} \frac{\nu_i}{A - g_i} \cos(g_i t + \beta_i) \tag{4.11b}$$

$$p_f(t) = -\sum_{i=1}^{N} \frac{\kappa_i}{B - f_i} \sin(f_i t + \gamma_i) \tag{4.11c}$$

$$q_f(t) = -\sum_{i=1}^{N} \frac{\kappa_i}{B - f_i} \cos(f_i t + \gamma_i) \tag{4.11d}$$

The frequencies g_i and f_i are the orbital precession frequencies for planet m_i, while the frequencies A and B are the so-called proper precession rates. The forced contributions h_f, k_f, *etc.*, are the forced motions that are excited by the perturbing planets, while e_p and I_p are the proper orbital elements and are unrelated to planetary perturbations, thus represent the grain's nascent radial

and horizontal velocity dispersion. Where we note that Eqns (4.10) can be used to determine the shape of the system's Laplace plane by setting both e_p and I_p to zero, and converting to Cartesian coordinates. Since Eqns (4.10) are a function of time, the Laplace plane will also be a function of time and the relevant timescale for the Laplace plane to change is the nodal precession frequency $2\pi/|f_i|$.

We also note that from these equations, one can see the artificiality of the initial conditions utilized in the models by Mouillet *et al.* (1997b). To produce the initial condition $I \simeq 0.0°$ for all the dust grains, I_p must conspire to exactly cancel the forced component of the inclination induced by a single planet (*i.e.* $I_p \simeq -I_f$). While this scenario is not impossible, as already mentioned, it is highly improbable.

From this point we can recover the traditional orbit elements via Eqns (4.1):

$$e = \sqrt{h^2 + k^2} \qquad \varpi = \tan^{-1}(h/k) \tag{4.12a}$$

$$I = \sqrt{p^2 + q^2} \qquad \Omega = \tan^{-1}(p/q) \tag{4.12b}$$

Chapter 5 then shows how we use these orbit elements to calculate a synthetic surface brightness map of a hypothetical dusty disk whose planetary parameters can be varied as the model image is fitted to the *HST* scattered-light image of β Pictoris.

Chapter 5

The Circumstellar Disk Model

As we saw in the previous chapter, it is possible to describe analytically the orbital evolution of a massless particle in the presence N massive bodies. This approach permits the rapid computation of the orbital position of millions particles, whereas other numerical methods (*e.g.* direct N-body methods) are limited to thousands of particles due to the large computational demands. Thus, our fast algorithm allows us to search efficiently a rather large parameter space for the orbits and masses of the planets that might be warping the β Pictoris disk. However, finding the set of parameters that best describe β Pictoris is non-trivial. This chapter will discuss our simulation process, as well as the method of determining the set of best-fitting model parameters.

5.1 The Model and Algorithm: `ringworld`

Dynamical modelling of dust clouds, such as the zodiacal cloud in the solar system, has been studied for years. As a result, many tools have been developed to facilitate this research [*e.g.* SIMUL by Dermott *et al.* (1989) and Xu *et al.* (1993)]. Since the aim of this study differs from others, we set out to write our own code: `ringworld`. This name was chosen to reflect the nature of our code, and the algorithm employed. Our code models the appearance of circumstellar disks in the presence of embedded planets (*i.e. worlds*), and we employ secular perturbation theory to describe the evolution of the system, which treats particles as narrow *rings*. The code is designed to generate a synthetic scattered-light image of a circumstellar disk, and search for the set of parameters that best describes the *HST* image of β Pictoris (Figure 2.1) provided by Heap *et al.* (2000).

To generate a synthetic scattered-light image, we first need to know how the dust grains are

spatially distributed. In our models, we assume the dust grains are randomly drawn from a radial power-law distribution. To populate the dust grains uniformly in a radial power-law distribution, we employ Monte Carlo simulation methods (Press *et al.*, 1992). In particular we use the transformation method, which relates a uniformly distributed random number to the desired probability function. This is accomplished by finding the inverse of the probability function's cumulative distribution function. To illustrate, we demonstrate this procedure for three different probability functions utilized in `ringworld`. We then describe how we generate a synthetic surface brightness map, search through parameter space and estimate parameter uncertainties.

5.1.1 Monte Carlo Simulation

We begin by deriving the generating function for the surface number density of dust grains. In the case of a single power-law distribution:

$$\sigma(a) = \sigma_0 \left(\frac{a_0}{a}\right)^{\alpha} \tag{5.1}$$

where a is the radial distance from the central star, and σ_0 is the surface number density of dust grains at some fiducial distance $a = a_0$.

For a surface number density $\sigma(a)$, the number of dust grains in an annulus of radius a and width da will simply be $dN(a) = 2\pi a\sigma(a)da$. Thus the fractional number of dust grains interior to a is given by:

$$\Sigma(a) = \frac{\int_{a_{min}}^{a} dN(a')}{\int_{a_{min}}^{a_{max}} dN(a')} \tag{5.2}$$

where a_{min} and a_{max} are the minimum and maximum radial distance from the central star.

If we let ξ be a random number that is uniformly distributed over (0,1), then we can interpret ξ as the probability that a given dust grain orbits interior to a. Solving $\xi = \Sigma(a)$ for a (*i.e.* $a = \Sigma^{-1}(\xi)$) yields the generating function for Eqn (5.1):

$$a(\xi) = \begin{cases} a_{min}\left(\frac{a_{max}}{a_{min}}\right)^{\xi} & \text{if } \alpha = 2, \\ \left[a_{min}^{2-\alpha} + \xi\left(a_{max}^{2-\alpha} - a_{min}^{2-\alpha}\right)\right]^{1/(2-\alpha)} & \text{if } \alpha \neq 2. \end{cases} \tag{5.3}$$

A more appropriate surface density distribution for the dust grains would be a broken power-law distribution, with at least two components. Justification for such a distribution comes from observations of the surface brightness profile of β Pictoris' mid-plane (see Figure 2.3). The above derivation can be extended to such a distribution, but we shall omit the result here.

Next we consider the nascent eccentricity and inclinations distribution (*i.e.* e_p and I_p), but for brevity we will only quote their respective probability and generating functions. According to Burns *et al.* (1979a), the proper eccentricity of the dust grains in the solar system follow a Rayleigh distribution:

$$f(e_p) = \frac{e_p}{\sigma_e^2} \mathrm{e}^{-e_p^2/2\sigma_e^2} \tag{5.4}$$

where σ_e is the dispersion of the distribution. Following the procedure outlined above, the generating function for a Rayleigh distribution is given by:

$$e_p(\xi) = \sigma_e \sqrt{-2 \ln[\{F(e_{min}) - F(e_{max})\}\xi - F(e_{min})]} \tag{5.5}$$

where $F(e_p) = -\mathrm{e}^{-e_p^2/2\sigma_e^2}$, while $e_{min} = 0$ and $e_{max} = 1$ are the minimum and maximum values of e_p.

The proper inclination distribution utilized by `ringworld` is a slightly more complicated function, which has been adapted from the projected vertical distribution described by Artymowicz *et al.* (1989) to the projected latitude distribution:

$$h(r, \theta) = \exp\left\{ - \left[\frac{\theta}{w(r)} \right]^{\gamma} \right\} \tag{5.6}$$

where γ controls the latitude distribution of the dust (*e.g.* $\gamma = 1$ for an exponential distribution and $\gamma = 2$ for a Gaussian distribution) and $w(r)$ is the latitudinal scale height

$$w(r) = w_0 \left(\frac{r}{r_0} \right)^{\delta} \tag{5.7}$$

where δ controls the flaring of the disk, and w_0 is the latitudinal scale height of the disk at $r = r_0$.

To obtain the proper inclination distribution $H(r, I_p)$ from the projected latitude distribution

$h(r,\theta)$, it was necessary to solve the integral equation (Brown, 2001):

$$h(r,\theta) = \int_{\theta}^{\pi/2} \frac{H(r,I_p)dI_p}{\sqrt{\sin {I_p}^2 - \sin\theta^2}} \tag{5.8}$$

However, an exact solution was not possible, but it was possible to compute an approximate solution to the proper inclination distribution (see Appendix D for details):

$$H(r,I_p) \simeq \frac{2}{\pi w(r)} \left(\frac{I_p}{w(r)}\right)^{\gamma-1} \mathrm{e}^{-[I_p/w(r)]^{\gamma}} \tag{5.9}$$

and following the procedure outlined above, the generating function is approximately given by:

$$I_p(r,\xi) \simeq w(r)[-\ln(\xi)]^{1/\gamma} \tag{5.10}$$

where it is assumed that $w(r) \ll 1$ for all our models.

5.1.2 Model Generation

To generate synthetic image of a circumstellar disk, `ringworld` requires several pieces of information, including: the radial dust distribution and the nascent eccentricity and inclination distributions of the dust grains (*i.e.* e_p and I_p). If massive bodies are present, then the masses and orbital elements of each body are also required. The procedure used by `ringworld` to generate a synthetic image is briefly summarized by the following nine steps that are implemented for each dust grain that is generated by this Monte Carlo model:

1. Use the Monte Carlo method of Eqn (5.15) to generate the dust grain's semi-major axis, a.

2. Calculate the dust grain's forced orbit elements: h_f, k_f, p_f and q_f, due to the planets' secular perturbations [see Eqns (4.11)].

3. Use Monte Carlo methods to determine the dust grain's proper eccentricity e_p and inclination I_p via Eqn (5.5) and Eqn (5.10), respectively.

4. Assume the dust grain's mean anomaly $\mathcal{M}$ is uniformly distributed over $0 < \mathcal{M} < 2\pi$, where $\mathcal{M} = nt$, n is the dust grain's mean motion, and t is the time since the dust grain's most

recent periapse passage. This is justified since the dust grains are assumed to be randomly distributed about their orbit, so t is arbitrary and hence the quantity $\mathcal{M}$ should be uniformly distributed about 2π. This same argument also applies to the the angular quantities $At + \varpi_p$ and $Bt + \Omega_p$ that appear in Eqns (4.10), so these angles are also randomized over 2π.

5. Calculate the dust grain's (h, k, p, q) orbit elements via Eqns (4.10), and convert to the familiar orbit elements (e, I, ϖ, Ω) via Eqns (4.12).

6. All of the grain's six orbit elements are now in hand: $a, e, I, \varpi, \Omega, \mathcal{M}$. These are then used to calculate the dust grain's Cartesian (x, y, z) position with respect to the central star, which is obtained by solving Kepler's equation numerically via the method described in Danby (1992).

7. Two angles are used to describe the orientation of the disk in 3–D space: I_{tilt}, the angle between the observer's line-of-sight and the disk mid-plane, and PA, the position angle of the disk's long axis relative to the *HST* image's CCD column. To account for the disk's orientation, we rotate the disk about the observer's line-of-sight by angle PA, and then tilt (*i.e.* rotate) the disk's mid-plane by angle I_{tilt}. This then yields each dust grain's new (x, y, z) coordinates in the observer's coordinate system, with the x-axis pointing towards the observer, and the y-z plane being the plane of the sky.

8. Calculate the scattering angle ϕ, which is the star-grain-observer angle. Then use the Henyey-Greenstein phase function to calculate the relative amount of light that the dust grain scatters to the observer:

$$\Psi(\phi) = \frac{1 - g^2}{4\pi(1 - 2g\cos\phi + g^2)^{3/2}} \tag{5.11}$$

where g is the asymmetry parameter, where $g = -1$ corresponds to perfect back-scattering, $g = 0$ for isotropic scattering, and $g = 1$ for perfect forward-scattering (Henyey & Greenstein, 1941). This particular phase function is used widely in studies of the zodiacal light (Hong, 1985), as well as for models of circumstellar disks (Kalas & Jewitt, 1995).

9. Add the scattered-light contributed by the dust grain, $F\Psi(\phi)$, to the synthetic image of the model disk. The scattered-light contribution $F\Psi(\phi)$ is the relative amount of starlight that the grain scatters towards the observer, where $F = L_\star/4\pi r^2$ and r is the distance from the star. This is accomplished by finding the pixel in the synthetic image that subtends the dust grain's coordinates (y, z) in the plane of the sky, and increment that pixel by $F\Psi(\phi)$.

5.1.3 Parameter Estimation

The minimization procedure employed here is the downhill simplex algorithm (Nelder & Mead, 1965; Press *et al.*, 1992). This algorithm requires $M+1 = 23$ distinct trial solution vectors as input, and the *simplex* refers to the vertices of the geometrical figure defined by these vectors in this M-dimensional parameter space. The elements of each vector are simply the M parameter values being considered for the trial solution vector (*i.e.* α, β, r_0, δ, γ, w_0, σ_e, g, I_{tilt}, PA and m_j, a_j, e_j, I_j, ϖ_j, Ω_j for $j = 1, 2$). The downhill simplex algorithm samples the χ^2 topography as it iteratively adjusts the simplex vertices and travels through the M-dimensional parameter space. The algorithm expands the simplex if it encounters a relatively flat χ^2 landscape, crawls downhill if it encounters a slope or a descending valley, and eventually contracts the simplex vertices about the deepest χ^2 minima it encounters. The downhill simplex method requires only function evaluations (*e.g.* χ^2), and not the calculation of derivatives. Due to this approach, the downhill simplex is not very efficient in terms of the number of function evaluations it requires to find a minima, but the computational burden is small and it is simple to implement. As a result of its nature, the downhill simplex method tends to get trapped in local minima. Performing numerous random restarts of the optimization process can alleviate this issue, which allows the simplex to sample more of the M-dimensional parameter space. Furthermore, these numerous restarts of the optimization process can also provide a crude statistical estimate of the parameter uncertainties.

To find the optimal parameter configuration, we carried out our Monte Carlo simulations making use of an adapted version of the well-known downhill simplex method in multi-dimensions

(AMOEBA) as described in Numerical Recipes in C (Press *et al.*, 1992). Specifically, we make use of the adaptation for the IDL programming environment which contains a few embellishments. The function we chose to minimize is the reduced χ^2 between the *HST* image of β Pictoris and our simulated image:

$$\chi_r^2(\mathbf{p}) = \frac{1}{N-M}\sum_{i=1}^{N}\left[\frac{f(x_i) - F(x_i;\mathbf{p})}{\sigma_i}\right]^2 \tag{5.12}$$

where σ_i is the standard deviation for the data point $f(x_i)$, while $F(x_i;\mathbf{p})$ is the model and $\mathbf{p}$ is the vector of M model parameters. The above sum is computed over all good *HST* pixels used in the fit (*i.e.* outside the masked region).

The AMOEBA algorithm stops when a given number of iterations is reached, or when the fractional deviation of the minimizing function drops below a given threshold. The starting points are randomly selected from a range of values for each of the dust and planetary parameters, where the ranges are determined using either physical arguments (*e.g.* $a > 0$ and $e > 0$) or external constraints (*e.g.* mass limits from radial velocity measurements). Since the result of one optimization depends greatly on the number of iterations and the values of the starting points, it becomes a non-trivial problem to find the right combination of starting values and iteration number, especially when each optimization takes a non-negligible amount of time. To provide an estimate of the number of iterations, we kept track of the value of χ_r^2 throughout the optimization process. It was found that after $\sim$200 iterations, the minimizing function did not change appreciable, so we fixed the number of iterations per optimization to 200.

To verify our two-planet hypothesis, we test both our planetless dust model (see §5.2) and two-planet model. The premise is that if the presence of planets improves the fit (*i.e.* decreases χ_r^2), then we can claim that our two-planet hypothesis is viable. The procedural steps outlined in the previous section are performed for 10^7 dust particles, but due to the nature of our image generation it is not necessary to compute all the orbits at once. We find that co-adding ten sets of 10^6 dust particles is near optimal, and does not place excessive demands on computer memory. The reason for such a large number of particles comes from the Monte Carlo nature of our image generation.

Though Monte Carlo methods are easy to implement, they are notoriously inefficient since they converge as $1/\sqrt{N}$ where N is the number of random numbers. This rate of convergence comes from the error estimate for Monte Carlo integration [see Eqn (7.6.1) in Press *et al.* (1992)]. However, we were limited to performing only 50 optimizations for both the dust and two-planet models. Even with the analytical nature of the solutions, the computational demand is sufficiently high that time constraints became an issue. To improve the convergence of the dust model and the two-planet model, we perform two passes with AMOEBA. In the second pass, the initial simplex is seeded using the top $M+1 = 23$ solutions returned from the first pass. In addition, the two-planet model is tempered by seeding the initial simplex with the best-fitting dust model parameters, which are then held fixed. Fixing the dust parameters increases the chances that AMOEBA will find an optimal solution, since the 200 iterations will now only try to improve the planetary parameters. For these secondary optimization runs we typically found that χ^2_r decreased, but not more than $\sim$3.

Now that the image generation and parameter estimation components of `ringworld` have been discussed, a test of its capabilities was designed. Since the warp feature in the β Pictoris disk is quite subtle, there was concern that AMOEBA would not be sensitive enough to find a solution. So a synthetic image of a circumstellar disk with a large warp was created, in the hopes that AMOEBA would be able to find the solution. The synthetic images makes use of the dust model described in §5.2.2, with the addition of two massive planets to produce the large warp. Since our concern was whether AMOEBA could recover the model parameters, a full parameter survey was not performed. Instead, only a single pass with ten optimizations were made, and where the initial simplex for each optimization was constructed by randomly perturbing the parameters for the synthetic data by 75%. To improve the probabilty of AMOEBA finding the correct solution, a number of the model parameters were held fixed (*i.e.* e_1, e_2, I_2, ϖ_1, ϖ_2 and Ω_2 as well as all the dust parameters). Ultimately, AMOEBA was able to obtain a best-fitting model with a $\chi^2_r = 2.81$. Figure 5.1 clearly show the excellent agreement between the synthetic data and the model, as well as the significantly warped spine of disk for the synthetic data. The best-fitting model parameters are listed below

Table 5.1: Summary of Two-Planet Model Fit to Synthetic Data

Parameter	Synthetic Data	Best-Fit
m_1 (M_J)[a]	15	16
m_2 (M_J)[a]	7.0	7.0
a_1 (AU)	50	66
a_2 (AU)	166	155
e_1	0.0[b]	0.0[b]
e_2	0.0[b]	0.0[b]
I_1 (°)	5.0	2.9
I_2 (°)	0.0[b]	0.0[b]
ϖ_1 (°)	0.0[b]	0.0[b]
ϖ_2 (°)	0.0[b]	0.0[b]
Ω_1 (°)	225	217
Ω_2 (°)	180[b]	180[b]

[a] M_J is the mass of Jupiter.

[b] Parameter is held fixed.

in Table 5.1, along with the parameters used to create the synthetic data. Upon comparison of the model parameters in Table 5.1, one can see that AMOEBA was able to recover the majority of the fitted parameters. Had more optimizations been used or a second pass been performed, the agreement could improve.

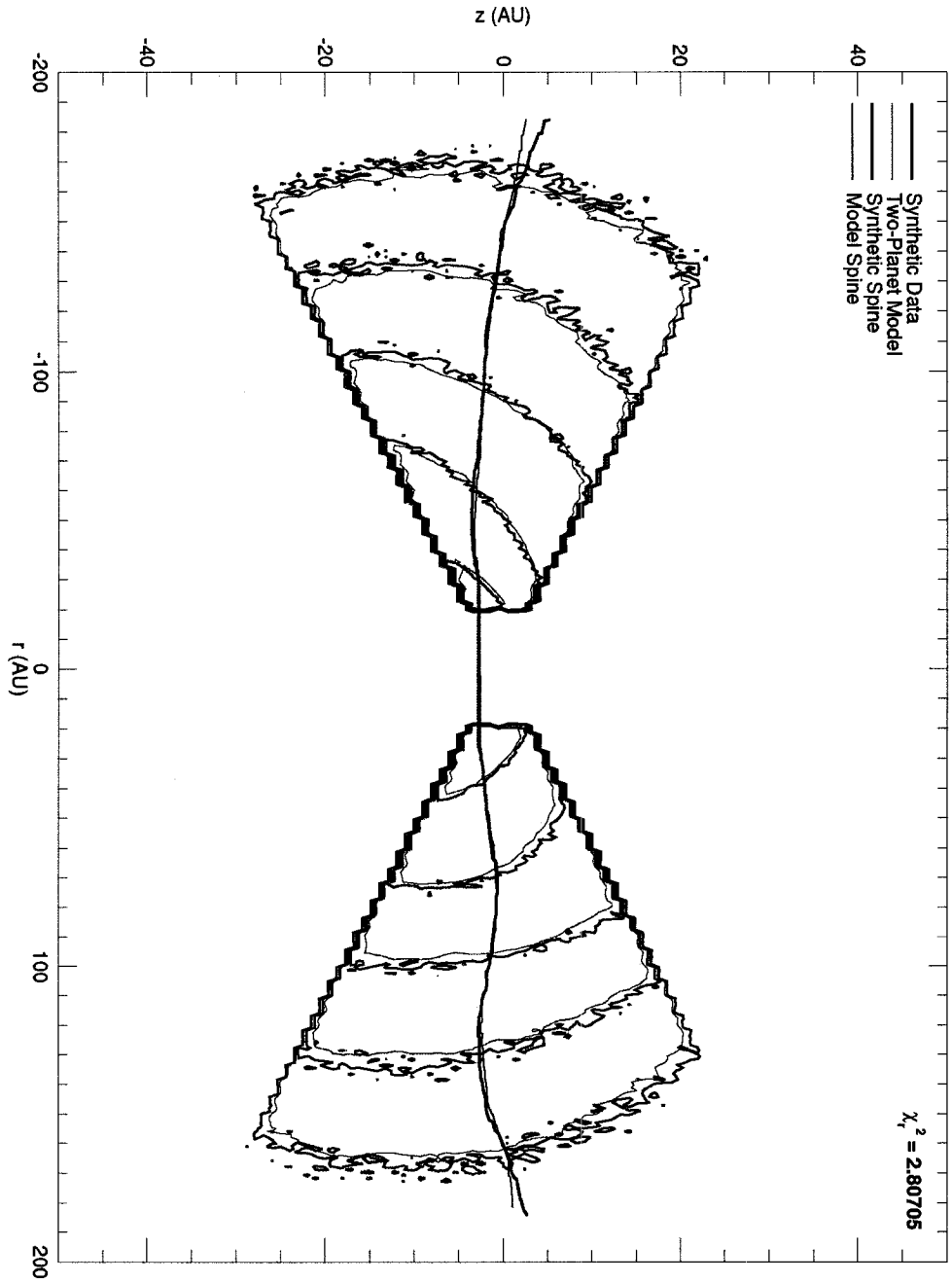

Figure 5.1: The best-fitting two-planet model to synthetic data, displayed with a vertical stretch. The spines for both images are generated by computing the vertical and horizontal centre-of-brightness of 100 isophotes for each extension, spaced logarithmically in brightness.

5.1.4 Error Analysis

As already indicated in the previous section, performing numerous optimizations can be used to estimate statistically the parameter uncertainties. This is accomplished by making a correlation between the range of χ_r^2 values and the range of parameter values returned by AMOEBA, in other words determine the parameter dispersion $\sigma(\mathbf{p})$ that satisfies the relation:

$$\chi_r^2(\mathbf{p}) \leq \chi_{r,min}^2 + \sigma_r(\mathbf{p}) \tag{5.13}$$

where $\chi_{r,min}^2$ is the minimum χ_r^2 returned by AMOEBA, and $\sigma_r(\mathbf{p})$ is the dispersion of χ_r^2 values. This statistical approach requires that a large number of optimizations be performed (*e.g.* $N_{opt} \gtrsim 10^3$). However, time constraints limited our number of optimizations to 50 for both the dust model and the two-planet model. Statistical analysis on such a small dataset would yield very unreliable parameter uncertainties, so more optimizations are needed to make use of this statistical approach.

However, we can still estimate the parameter uncertainties by noting how far each parameter must be perturbed to increase χ_r^2 by a certain amount, *i.e.*

$$\chi_r^2(\mathbf{p}') = \chi_{r,crit}^2 \tag{5.14}$$

where $\mathbf{p}'$ is the perturbed solution vector, and $\chi_{r,crit}^2$ is the χ_r^2 threshold. We find that searching for parameters that double the minimum χ_r^2 is a reasonable criterion, so we set $\chi_{r,crit}^2 = 2\chi_{r,min}^2$.

It is worth noting that while the $\chi_{r,crit}^2 = 2\chi_{r,min}^2$ criterion is completely arbitrary, there is a justification for this choice. In our investigation, it was quickly realized that χ_r^2 varied considerably even when the parameters did not change appreciably or when they were held fixed (see Figure 6.2). It was observed that these χ_r^2 variations could be as large as $\sim 1.2\chi_{r,min}^2$, but they could extend out to $\sim 1.5\chi_{r,min}^2$. We identified the culprit as the random seed used in our Monte Carlo image generation, which is initialized with the computer's system time each time an image is generated. To ensure we can distinguish between these intrinsic χ_r^2 variations and any variation due to changes to a model parameter, the threshold $\chi_{r,crit}^2 = 2\chi_{r,min}^2$ was chosen. Furthermore, since it was not

possible to derive a direct relation between χ^2_r uncertainties with parameter uncertainties, we have opted for this approximate approach.

With this criteria in place, we searched for the value of $\mathbf{p}'$ using the bisection method which guarantees finding a solution, so long as the two starting points bracket $\mathbf{p}'$. Searching about each best-fitting parameter, we estimated the uncertainty in the i^{th} parameter p_i to be $\sigma(p_i) = |p_{i,max} - p_{i,min}|/2$, where $p_{i,max}$ and $p_{i,min}$ are the two possible roots of Eqn (5.14). In the event that only $p_{i,max}$ or $p_{i,min}$ could be found, we then estimated the parameter uncertainty as $\sigma(p_i) = |p_{i,max} - p_i^*|$ or $\sigma(p_i) = |p_i^* - p_{i,min}|$, where p_i^* is the best-fitting value for the parameter p_i.

5.2 The Dust Models

5.2.1 A Simple Dust Model

As a starting point, we attempted to fit the simplest possible planetless dust-disk model to the *HST* observations of β Pictoris (see Figure 2.1). For this simple model, we assume the radial distribution of dust grains follow a single power-law distribution as described by Eqn (5.1). For the proper eccentricity and inclination distributions, we assume that they both follow a Rayleigh distribution as described by Eqn (5.4). Finally, for the light scattering distribution, we use the Henyey-Greenstein phase function as described in Eqn (5.11).

We performed a preliminary parameter search using AMOEBA, and the model did not show good agreement with the *HST* data as evidenced by the large value of $\chi^2_{r,min} = 19.81$. This simple dust model failed to replicate accurately the appearance of β Pictoris in scattered-light, and the inadequacy of this model is also evident from visual inspection of Figure 5.2. The isophotes of β Pictoris are angular in shape, whereas the isophotes for the simple dust model are more rounded. Furthermore, the steep decline in surface brightness beyond ~100 AU is also not accurately modelled. Also plotted are the spines of the disk for β Pictoris and our model, which are generated by computing the vertical and horizontal centre-of-brightness of 100 isophotes for each extension, spaced

logarithmically in brightness. As we can see as well, the spine for β Pictoris and the model also do not agree. The poor agreement with this model can be attributed to its simplistic parameterization, which is inadequate to describe some of the more salient features of β Pictoris' disk. This motivates us to find a more appropriate dust model that can satisfactorily characterize the β Pictoris disk.

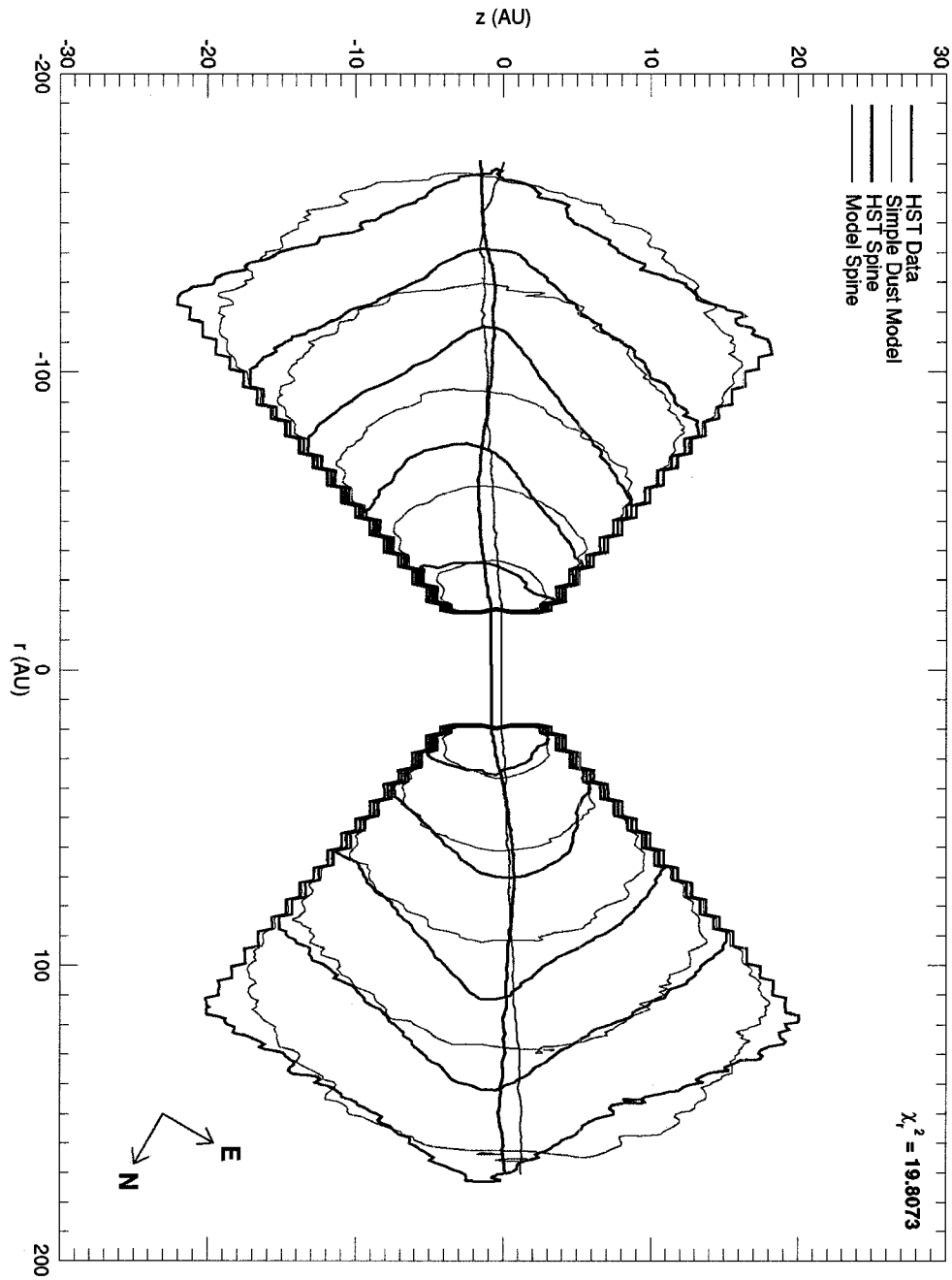

Figure 5.2: The best-fitting simple dust model superimposed over the β Pictoris data, displayed with a vertical stretch. The spines for both images are generated by computing the vertical and horizontal centre-of-brightness of 100 isophotes for each extension, spaced logarithmically in brightness.

5.2.2 The Artymowicz Dust Model

Since the single power-law disk provides a poor fit to the observed surface brightness map, we will now adopt a broken power-law with two different exponents for the radial dust distribution. This radial surface density is now governed by three parameters, α, β and r_0:

$$\sigma(r) = \sigma_0 \begin{cases} (r_0/r)^{\alpha} & r_{min} \leq r \leq r_0 \\ (r_0/r)^{\beta} & r_0 \leq r \leq r_{max} \end{cases} \tag{5.15}$$

where r_0 is the transition radius, while $r_{min} = 20$ AU and $r_{max} = 250$ AU are the inner and outer edge of the disk. These values are set by the physical scale of the image at the distance of β Pictoris, and the size of the software mask for the inner edge and the maximum extent of the *HST* image for the outer edge.

The main difference between this model and the simple dust model lays in the description of the proper inclination distribution, which we adapt from Artymowicz *et al.* (1989). In §5.1.1 we reported the generation function for the proper inclination distribution in Eqn (5.10), which is derived in detail in Appendix D. For the lack of a better description, we shall continue to use Eqn (5.5) and Eqn (5.11) for the proper eccentricity and light scattering distributions, respectively. This dust model has more adjustable parameters than the simple dust model, which allows it to describe the general features in the *HST* image of β Pictorismore accurately. As we will see in §6.1, this dust model indeed does a better job since it significantly decreases the χ^2_r of the fit.

Chapter 6

The Parameter Search

In this chapter we report the results of our parameter surveys for both the planetless Artymowicz dust model, and the two-planet model. The parameter uncertainties reported are computed using the prescription outlined in §5.1.4, and represent a crude estimate of a model's sensitivity to its parameters.

6.1 Results for the Dust Model

Using the Artymowicz dust model, we performed a parameter search to fit the large-scale features in the *HST* image of β Pictoris. For the AMOEBA routine, an initial simplex is required to provide a starting point for the parameter search. The initial simplex for each optimization is constructed by randomly drawing each parameter from some uniform distribution. Since *a priori* knowledge of the possible parameter ranges are not available for all the parameters, those parameter ranges were given a wide girth to circumvent our ignorance.

To refine our results further and ensure that we have converged to the best solution, a second parameter search was performed using the results of the first search to seed each initial simplex for this second pass. From results of this second optimization pass, we find the best-fitting dust model has a $\chi^2_r = 10.4$, which would be smaller using the real error map. The dust model in Figure 6.1 shows modest agreement with the *HST* data, but displays significant improvement over the simple dust model. While the Artymowicz dust model is able to better characterize the brightness distribution of β Pictoris, it is not able to reproduce the warp as seen in the spine of the *HST* image. The best-fitting model parameters are listed in Table 6.1, along with the model parameters

determined by Kalas & Jewitt (1995) for a similar dust model. The two sets of model parameters in Table 6.1 show reasonable agreement, except for two notable exceptions: α and β. The discrepancy in β is because the model is not very sensitive to the value of β, which is the power-law exponent in the outer disk (*i.e.* $r > 100$ AU). Figure 6.1 suggests the model is only fitting to data out to a projected distance of $r \sim 150$ AU, and at that distance, the disk's surface brightness has only just started to steepen. Thus the model recovered the wrong value for β, one that is too shallow. Perhaps if the data covered a wider range of project distances, the model would be more sensitive to the value of β. The discrepancy in α is the more vexing of the two, and the source of its discrepancy is not exactly known. Extensive testing of `ringworld` reveals that for special cases, the code produces the expected results. In the case where the latitudinal scale height $w_0 = 0$, the radial dependence of the synthetic images agreed with analytical models. However, when $w_0 \neq 0$ the radial dependence of the synthetic models were steeper than expected. Changes to δ or γ did not appreciably alter the results.

It was noticed that through the course of our investigation, that the χ_r^2 varied considerably even when the parameters did not change appreciably or were held fixed. To illustrate this phenomenon, 10^3 χ_r^2 values were computed using the same set of dust parameters. The result can be seen in Figure 6.2, which shows a histogram of the χ_r^2 values. The distribution spans almost $\sim$1 in χ_r^2, and has a standard deviation of $\sim$0.2 about the median value. After ruling out all other possible sources, we arrived at the conclusion that these variations are due to our Monte Carlo image generation. This is quite problematic, since it introduces an uncertainty in the determination of the best-fitting model parameters. An obvious remedy to this problem would be to use more particles in the simulation or more iterations per optimization, but this is not a practical solution for reasons already mentioned. Another possible solution would involve fixing the random seed used in the model image generation, so that all the models will use the same set of random numbers. However, at the time of the discovery of this problem, a large fraction of our results had already been completed. Furthermore, time constraints did not permit us to perform our parameter searches again using a fixed random

seed.

To illustrate this phenomenon further, we draw a large set of random numbers are from a simple linear model [*i.e.* $x = \sqrt{\xi}$, where ξ is a uniformly distributed random number on (0,1)]. Displayed in each panel of Figure 6.3 is a normalized histogram (the thin black line) for increasing values of the number of particles N_{part}, and the linear model (the thick red line). Each histogram has 100 equally spaced bins, and $N_{part} = 10^3$ for the top left panel and increases from left to right, and top to bottom in powers of 10. The χ^2_r is computed between each normalized histogram and the linear model with a constant uncertainty of $\sigma = 0.0075$, and is displayed on the top left corner of each panel. Figure 6.3 shows the rate of convergence of Monte Carlo simulations, and illustrates why such a large number of particles are required in our simulated images. In each panel of Figure 6.4 is a histogram of χ^2_r values for the corresponding values of N_{part} in Figure 6.3, and each histogram is computed for 10^3 iterations each using a different random seed. Figure 6.4 shows how the dispersion of these distributions decreases with increasing N_{part}, and illustrates that for fixed model parameters the χ^2_r values have a range of values. The lack of *a priori* knowledge of the mean $\langle\chi^2_r(\mathbf{p})\rangle$, and the dispersion $\sigma_r(\mathbf{p})$ of these distributions as a function of $\mathbf{p}$ and N_{part} are what makes the issue of χ^2_r variations so vexing. By fixing the random seed would select only one value of χ^2_r from the histograms in Figure 6.4, and thus provide a one-to-one correspondence between $\mathbf{p}$ and χ^2_r for a given value of N_{part}. While our results should not depend on the random seed, the analysis illustrates that only in the limit of extremely large N_{part} is this truly the case. So while fixing the random seed should be avoided, it does circumvent the issue of χ^2_r variations for smaller values of N_{part}.

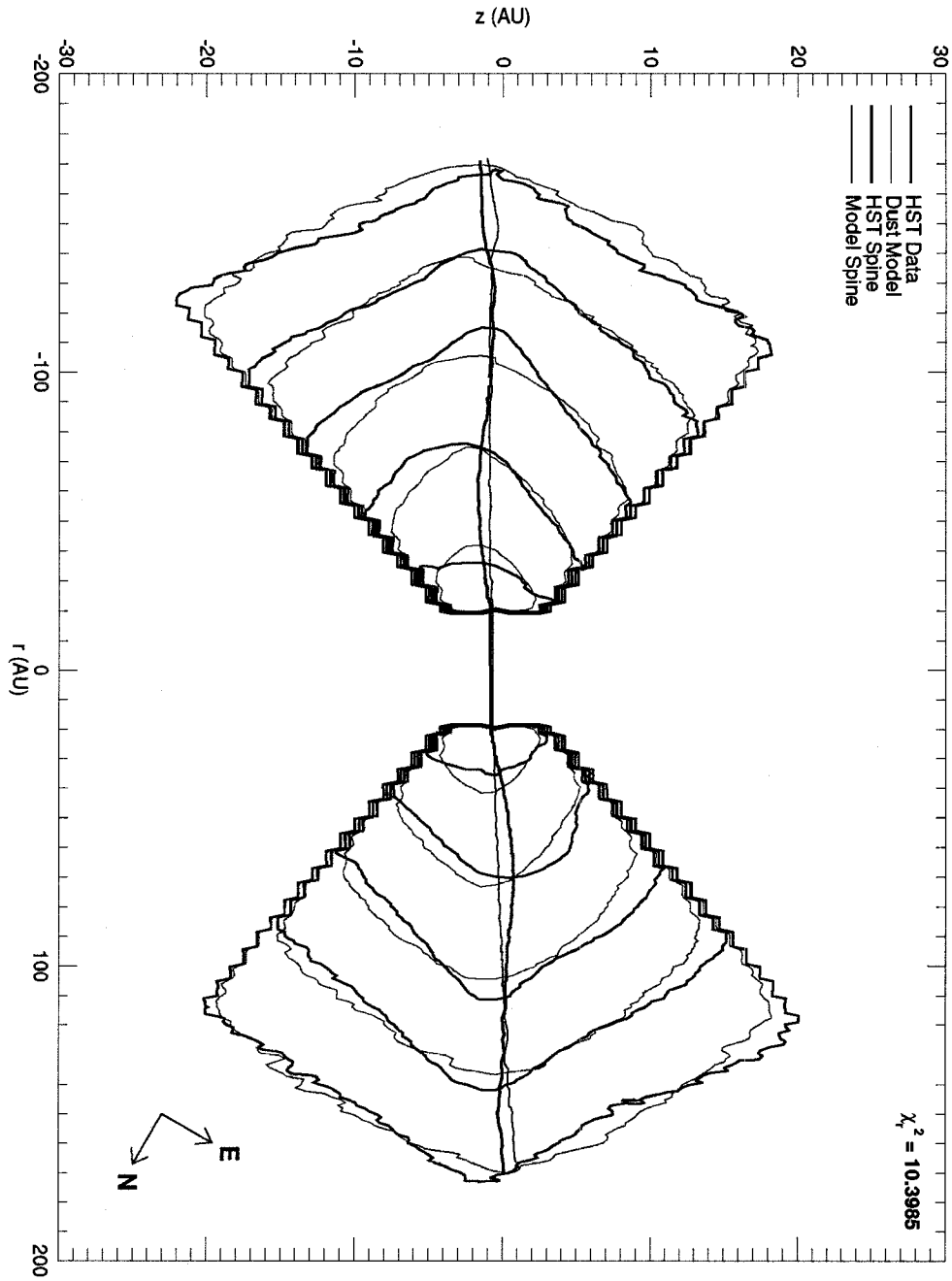

Figure 6.1: The best-fitting Artymowicz dust model superimposed over the β Pictoris data, displayed with a vertical stretch.

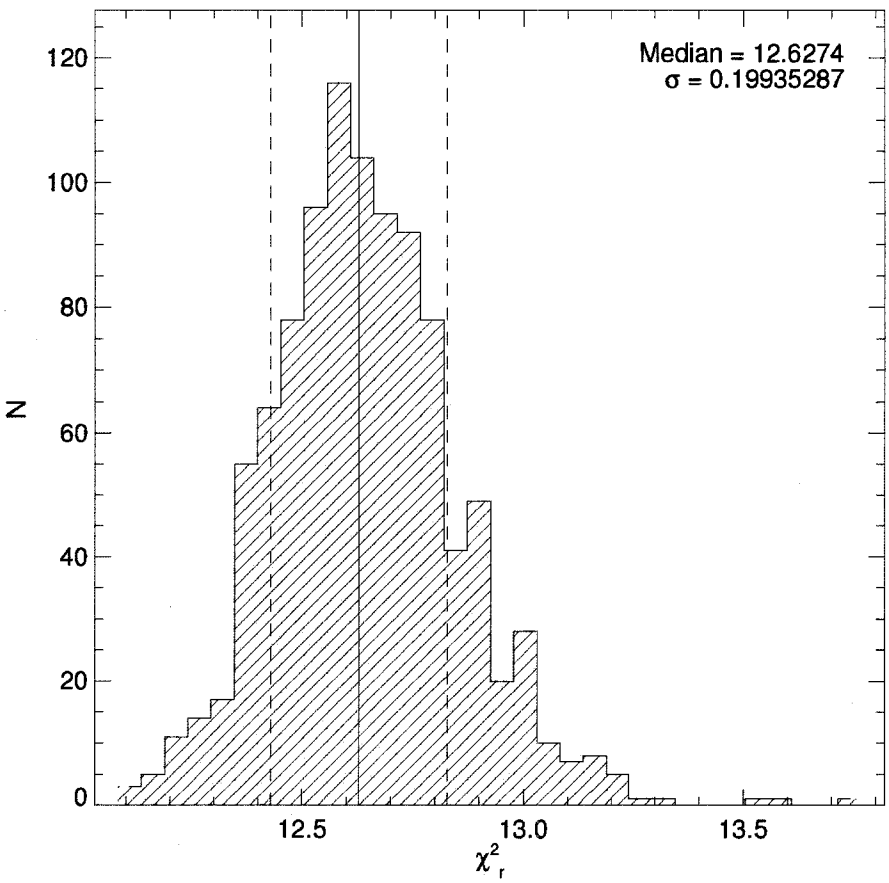

Figure 6.2: Histogram of χ^2_r variations for fixed dust model parameters. See text for details.

Table 6.1: Comparison of the Dust Model Parameters

Parameter	Kalas & Jewitt (1995)	Best-Fit
α	0.45 ± 0.3[a]	-1.07 ± 0.23
β	1.75 ± 0.3[a]	0.60 ± 0.80
r_0 (AU)	116[b]	95 ± 13
δ[c]	0.35 ± 0.25	0.05 ± 0.37
γ	1.35 ± 0.65	1.5 ± 0.36
w_0[d]	0.08 ± 0.02	0.13 ± 0.03
σ_e	...	$0.01^{+0.07}_{-0.00}$
g	0.4 ± 0.1	0.43 ± 0.08
I_{tilt} (°)	3.5 ± 1.5	1.60 ± 0.02
PA (°)	...	-0.44 ± 1.15

[a]To compare the radial power-law exponents, we integrate the volume number density $n(r, z)$ of Kalas & Jewitt (1995) over z to obtain a surface number density *i.e.* $\sigma(r) = 2\int_0^\infty n(r, z)dz$. This decreases both exponents reported in Kalas & Jewitt (1995) by $\delta = 1.35$.

[b]The transition radius is fixed at $6'' \sim 116$ AU.

[c]Our flare index δ differs from the index β' used in Kalas & Jewitt (1995) by one *i.e.* $\delta = \beta' - 1$.

[d]Our latitudinal scale height $w_0 = \zeta_0/r_0$, where ζ_0 is the vertical scale height from Kalas & Jewitt (1995).

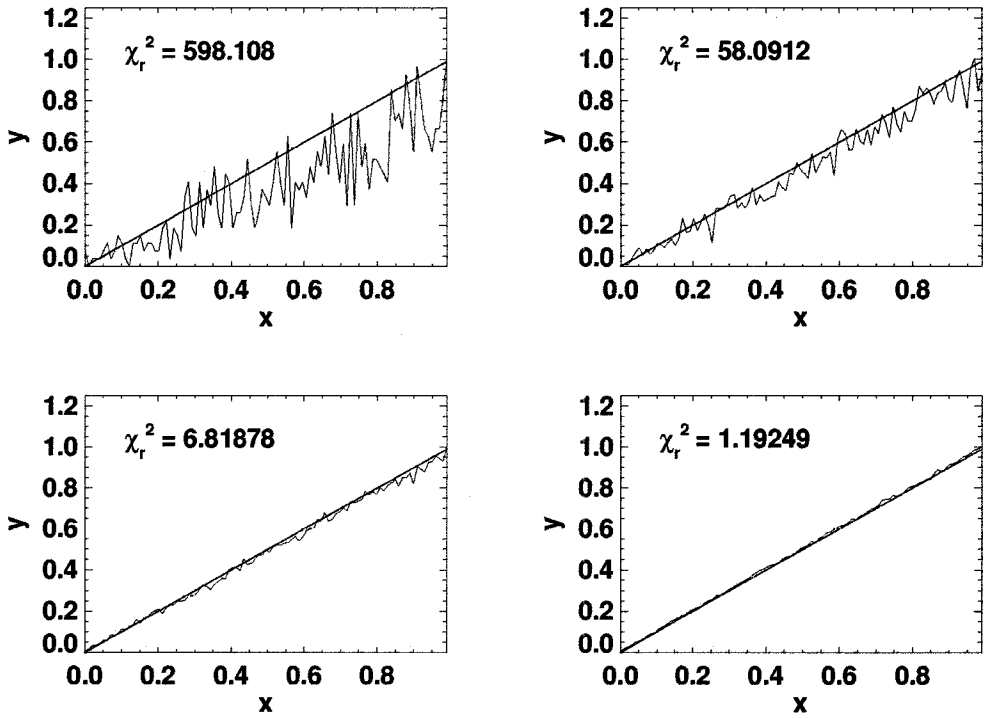

Figure 6.3: Plotted in each panel is a simple linear model (thick red line), and a normalized histogram (thin black line) of N_{part} random numbers drawn from the linear model. The top left panel has $N_{part} = 10^3$, and increases from left to right, and from top to bottom in powers of 10. The displayed value of χ_r^2 is computed between the normalized histogram and the linear model (see text for details).

6.2 Results for the Two-Planet Model

With the best-fitting dust model in hand, we now attempt to fit the *HST* image of β Pictoris by including two planets. We follow the same procedure outlined in the previous section on generating the initial simplex for AMOEBA, but we fix all the dust parameters to the best-fitting model reported in Table 6.1. We also had the same issue with the possible parameter ranges used to create the initial

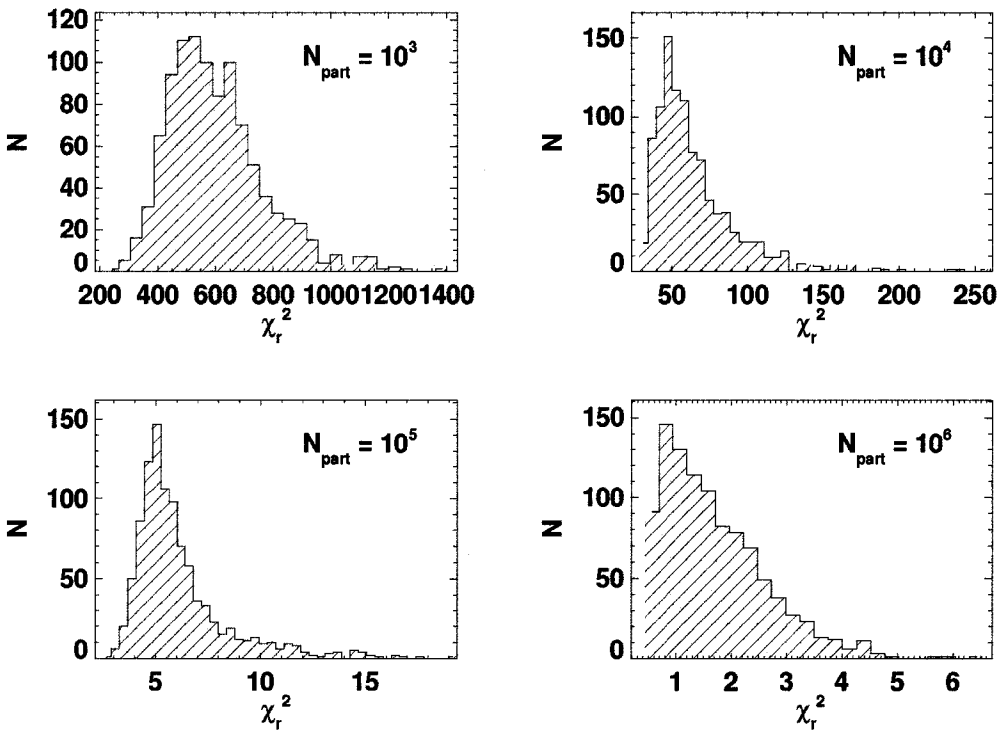

Figure 6.4: Histograms of χ_r^2 values computed using different random seeds for the corresponding panels in Figure 6.3

simplex, so we similarly gave each parameter a wide range. The χ_r^2 variations are still an issue, and we will discuss some simple remedies in §7.1.

We refined our results by performing two optimization passes, seeding the initial simplex of the second pass with the best results of the first. From results of this second optimization pass, we find the best-fitting two-model has a $\chi_r^2 = 9.84$. In Figure 6.5, we can see the agreement is much better than the simple dust model, and there is even some improvement over the Artymowicz dust model. The contours show good agreement, and the spines almost completely overlap except beyond ~140 AU where they diverge. A possible reason for this disagreement could be the small number of particles available at these large distances from the star. As a result, the calculation of the centre-of-brightness based on these small number of particles will be increasingly susceptible to any

pixel-to-pixel variations. The best-fitting model parameters are listed in Table 6.2, along with a set of model parameters rotated to a reference plane perpendicular to the plane of the sky. The model parameters are measured with respect to the reference plane that lies in the disk's mid-plane, far from the planets (*i.e.* $r \gg 200$ AU). The disk mid-plane is not oriented perpendicular to the plane of the sky since $I_{tilt} \neq 0$, which means the x-axis in the system's reference frame does not point exactly along the observer's line-of-sight. In the rotated reference frame, the y'-z' plane is parallel to the plane of the sky and the x'-axis now points along the line-of-sight. To write the parameters to the rotated reference frame, they were first converted to the Cartesian coordinates assuming the mean anomaly is $\mathcal{M} = 0$ for each planet. Then they were rotated about the system's x- and y-axes by $-PA$ and $-I_{tilt}$, respectively. Then they were converted back to orbital elements. Since I_{tilt} and PA are both small, the majority of the planetary parameters did not change very much. Based on best-fitting two-planet configuration, the Laplace plane responsible for this warp is stable over $2\pi/|f_2| \simeq 7.9$ Myrs, where f_2 is the nodal precession frequency of the outer planet.

A note about the lack of error estimates for the three parameters: ϖ_1, ϖ_2 and Ω_2. In the case of ϖ_1 and ϖ_2, it was not possible to satisfy the $\chi^2_{r,crit}$ chosen for our error analysis because of the small eccentricity of each planet *i.e.* $e_1 = 0.04$ and $e_2 = 0.04$. For a circular or nearly circular orbits, the periapse direction ϖ becomes indeterminate. Similarly, Ω becomes indeterminate when I gets very small. In both cases, this indeterminacy translates into the two-planet model becoming insensitive to the variation of ϖ_1, ϖ_2 and Ω_2. The only exception here is Ω_1. Both I_1 and I_2 are $\lesssim 3°$, and yet it was possible to provide an error estimate for Ω_1. The reason for this discrepancy comes from the larger mass for the inner planet, which will have a larger influence as a consequence, so the two-planet model will still be sensitive to any variations in Ω_1.

To illustrate our confidence in the two-planet model, we generate 100 models randomly perturbed by the errors reported in Table 6.2 about the best-fitting two-planet model. We plot just the spines of the perturbed models in Figure 6.6, along with the spine of the best-fitting two-planet model and the spine of β Pictoris. Upon inspection of Figure 6.6, we note that the majority of the perturbed

spines are localized in a narrow band about both the spine of the best-fitting two-planet model and the spine of β Pictoris. From this visual inspection of the perturbed spines, we can conclude that the parameter error estimates provide a reasonable estimate of our model uncertainties.

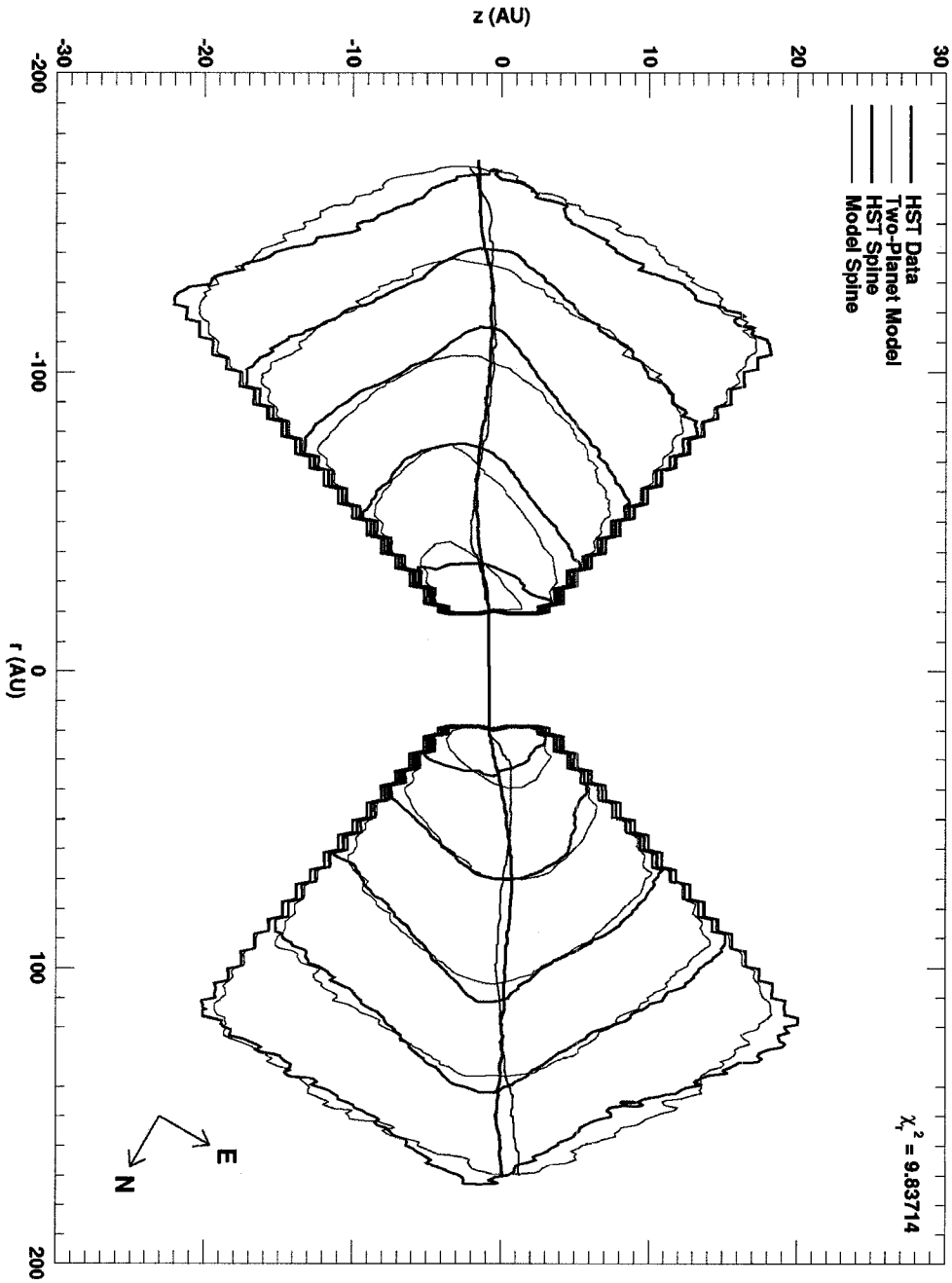

Figure 6.5: The best-fitting two-planet model superimposed over the β Pictoris data, displayed with a vertical stretch.

Table 6.2: Summary of Two-Planet Model Parameters

Parameter	Best-Fit (System)[a]	Best-Fit (Rotated)[b]
m_1 (M_J)[c]	6.8 ± 4.3	6.8 ± 4.3
m_2 (M_J)[c]	3.3 ± 0.8	3.3 ± 0.8
a_1 (AU)	35 ± 11	35 ± 11
a_2 (AU)	131 ± 41	131 ± 41
e_1	$0.04^{+0.23}_{-0.00}$	$0.04^{+0.23}_{-0.00}$
e_2	$0.04^{+0.28}_{-0.00}$	$0.04^{+0.28}_{-0.00}$
I_1 (°)	$2.6^{+5.4}_{-0.0}$	1.9 ± 1.5
I_2 (°)	$2.3^{+5.0}_{-0.0}$	3.8 ± 3.6
ϖ_1 (°)	184[d]	186[d]
ϖ_2 (°)	178[d]	178[d]
Ω_1 (°)	140 ± 55	178 ± 75
Ω_2 (°)	241[d]	252[d]

[a]The reference frame adopted here has its x-y plane in the disk's midplane, far from the planets (*i.e.* $r \gg 200$ AU).

[b]This reference frame has its x'-y' plane perpendicular to the plane of the sky.

[c]M_J is the mass of Jupiter.

[d]No error estimate possible.

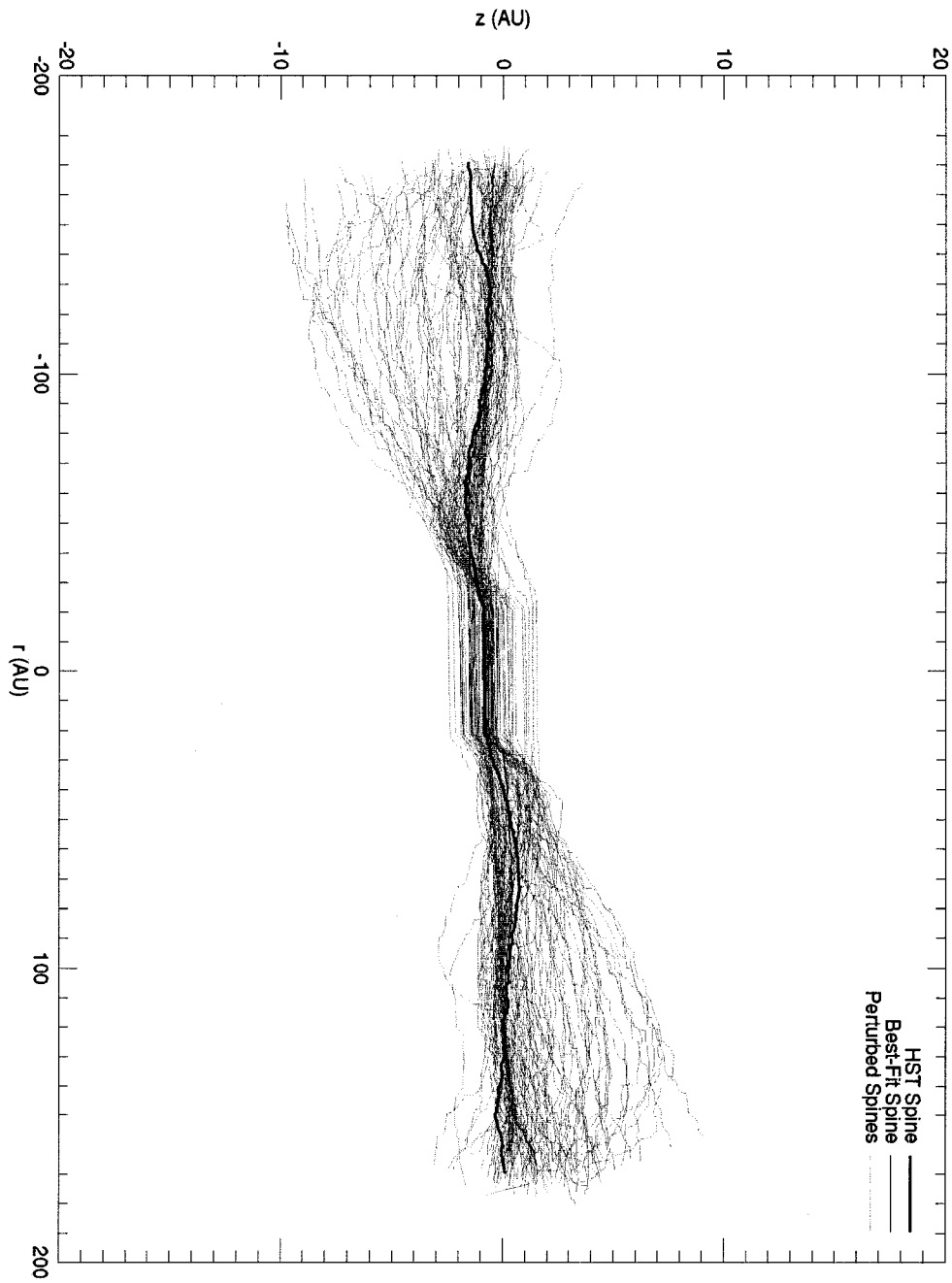

Figure 6.6: The spines of randomly perturbed best-fitting two-planet model, along with the best-fitting two-planet spine and the β Pictoris spine superimposed.

Chapter 7

Conclusion

The results of this study presented in §6 show good agreement with the *HST* image of β Pictoris, both for the dust model and the two-planet model. The addition of two planets to the dust model was able to decrease the χ_r^2 from 10.40 to 9.84, but whether this change is significant enough to conclusively claim that our two-planet model correctly describes the data is debatable. However, the warped spine of the β Pictoris disk is more accurately described when the two planets are included. So while the inclusion of two planets did not result in a substantial decrease in χ_r^2, our two-planet model is able to reproduce the warp seen in the *HST* image of β Pictoris.

There are several possible reasons why χ_r^2 did not decrease significantly with the two-planet model, and chief among them is the limited number of optimizations. With our small number of optimizations, there is a very real possibility that our results represents only a local minimum in the χ_r^2 topography. Other possible reasons include the χ_r^2 variations, and the number of particles used to simulate the disk. Increasing the number of particles would obviously be desirable, but time constraints and computational resources placed hard limits on the number of particles that can be used in our simulations.

If we are ultimately able to claim the two-planet model correctly describes the data, then our approach would provide a litmus test for the presence of embedded planets in circumstellar dust-disks. Such a tool could then be used to study other systems with a known circumstellar dust-disk (*e.g.* HR4796A, Fomalhaut, AU Microscopii, *etc.*) for the presence of planets.

7.1 Future Work

There are several different possibilities for future work on the β Pictoris system. The next logical step would be to fit simultaneously multiple wavelength data (*e.g.* optical, infrared, sub-mm, *etc.*). Observing at various wavelengths means that one is viewing different-sized dust grains; because one would be observing the most abundant dust grains visible at a given wavelength. According to scattering theory (Taylor, 1972), the dominant scattering particles in a population will be those that have sizes comparable to the wavelength of observation (particles much smaller than the wavelength will be largely invisible to the observer). Thus a multi-wavelength observations will be sensitive to the dust size distribution. While modelling of the dust size distribution would add more parameters to the model, the possibility of placing more constraints on other parameters (*e.g.* the planetary parameters) would out-weigh any issues dealing with a dust grain size distribution. In particular, potential follow-up work could make use of recent mid-infrared observations made by Telesco *et al.* (2005), which could help provide additional constraints on the masses, semi-major axis and eccentricity of any planets.

However, large improvements can be made without new data; increasing the speed and efficiency of `ringworld` would be the largest single improvement. A significant speed increase would permit the computation of more models, thereby increasing the statistical significance of any solution. One could also increase the number of particles used to generate the synthetic images, and avoid placing large fractions of the particles behind the image mask. A crude estimate gives the current percentage of particles laying behind the mask at ~50%-60%, so any effort to construct an image that lowers this fraction will ultimately increase the signal-to-noise of the synthetic image outside of the mask. Furthermore, the Monte Carlo simulation in `ringworld` uses a different random seed for each synthetic image, which introduces χ^2_r variations even when the model parameters are held fixed (see Figure 6.2). A simple remedy would be to use the same random seed for each synthetic image, so that all the models can be compared on the same footing and eliminating a source of uncertainty. While

the χ^2_ν variations would not prevent finding a solution, they would only frustrate the AMOEBA simplex algorithm. Increasing the number of iterations per optimization could alleviate this issue as well, but since it takes a non-trivial amount of time to generate a model image we have the same issue with time and computational constraints.

Another avenue being explored by the author is the combination of two different parameter searching algorithms, a genetic algorithm and simplex method as proposed by Charbonneau (1995). Genetic algorithms search for the set of best parameters using the principles of evolutionary biology: natural selection, genetic mutation and large populations. The advantage of genetic algorithms is their ability to find the *global* minima, unlike the simplex method which is essentially a *local* searching algorithm. A drawback of genetic algorithms is their slow rate of convergence to a solution, while the simplex method enjoys a comparatively rapid rate of convergence. A hybrid approach would make the best use of both methods: the global searching capability of genetic algorithms and the rapid convergence of the simplex method. Specifically, the genetic algorithm would be used first to survey the parameter space to assess its global structure. Then a subset of the best solutions returned by the genetic algorithm would be used to seed the simplex, which would then rapidly convergence to a solution.

Appendix A

Acceleration Due to a Ring

In this section we derive the acceleration that a particle of mass m' exerts on another particle of mass m.

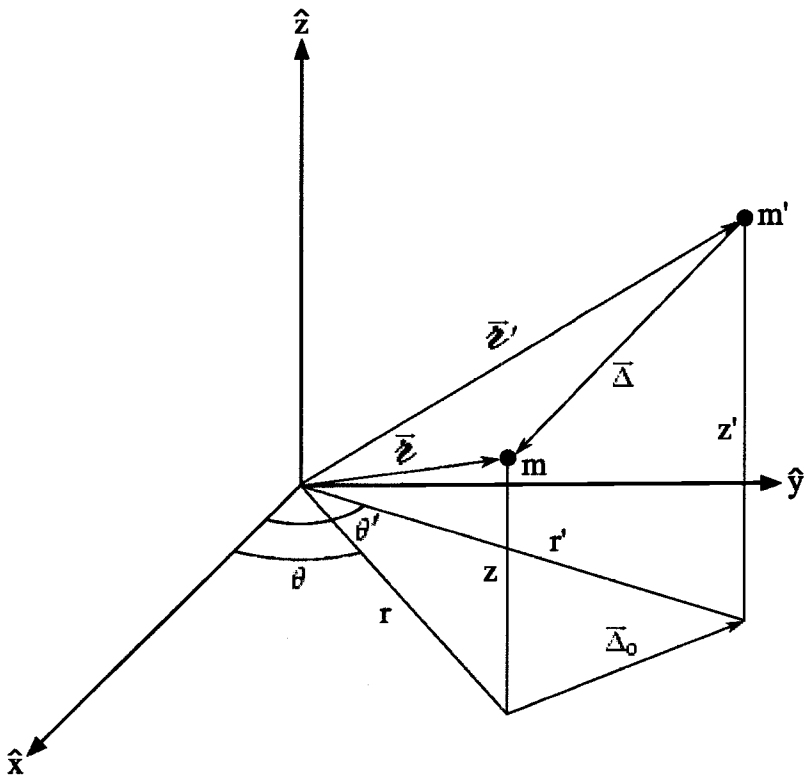

Figure A.1: The two-body configuration

We begin by writing the gravitational potential that m experiences due to the perturbing particle m':

$$\Phi(\vec{r}) = -\frac{Gm'}{\Delta} \tag{A.1}$$

where the separation vector $\vec{\Delta} = \vec{r} - \vec{r}'$ points from m' to m, and $\Delta = |\vec{\Delta}|$.

Since the separation between m and m' is $\Delta = \sqrt{\Delta_0^2 + (z - z')^2}$, we can write (A.1)

$$\Phi(\vec{r}) = -\frac{Gm'}{\Delta_0}\left[1+\left(\frac{z-z'}{\Delta_0}\right)^2\right]^{-1/2} \tag{A.2}$$

where $\Delta_0 = \sqrt{r^2 - 2rr'\cos(\theta - \theta') + r'^2}$ is the separation between m and m' projected onto the $\hat{x}$-$\hat{y}$ plane.

We can linearize our equations of motion by assuming that the bodies vertical separations are small compared to their horizontal separations *i.e.* $|z - z'| \ll \Delta_0$, so

$$\Phi(r, \theta, z, t) \simeq \Phi_0(r, \theta, t) + \Phi_z(r, \theta, z, t) \tag{A.3}$$

where Φ_0 and Φ_z are

$$\Phi_0(r, \theta, t) = -\frac{Gm'}{\Delta_0} \tag{A.4a}$$

$$\Phi_z(r, \theta, z, t) = \frac{Gm'}{2\Delta_0^3}(z - z')^2 + \mathcal{O}(z - z')^4 \tag{A.4b}$$

where the Φ_0 potential is the zeroth-order term that tells us about the radial and tangential forces exerted on m, while the Φ_z potential is the lowest-order term that carries information about any vertical forces. The Cartesian components of the acceleration due to m' are derivatives of Φ_0 and Φ_z:

$$a_x \simeq -\frac{\partial \Phi_0}{\partial x} \tag{A.5a}$$

$$a_y \simeq -\frac{\partial \Phi_0}{\partial y} \tag{A.5b}$$

$$a_z \simeq -\frac{\partial \Phi_z}{\partial z}. \tag{A.5c}$$

Next, Fourier expand Φ_0 and Φ_z:

$$\Phi_0(r, \theta, t) = \frac{1}{2}\phi_0(r) + \sum_{k=1}^{\infty} \phi_k(r)\cos[k(\theta - n't)] \tag{A.6a}$$

$$\Phi_z(r, \theta, z, t) = \frac{1}{2}\phi_{z,0}(r, z) + \sum_{k=1}^{\infty} \phi_{z,k}(r, z)\cos[k(\theta - n't)] \tag{A.6b}$$

where $n' = \sqrt{G(M_\star + m')/a'^3}$ is the average angular velocity of m' about the primary $M_\star$, while $\phi_k(r)$ and $\phi_{z,k}(r, z)$ are the amplitude of the k^{th} Fourier component of Φ_0 and Φ_z, respectively.

In the above Fourier expansions, the $k \geq 1$ time dependent terms describe the evolution of the gravitational perturbation experienced by m due to m'. Since m and m' orbit the central star at the average angular rates n and n' respectively, the gravitational perturbation that m will experience will vary with a period $T = 2\pi/|n - n'|$. If the mean angular velocities of m and m' are commensurable (*i.e.* n/n' is a ratio of whole numbers), then the two bodies reside in a mean-motion resonance. In the language of galactic dynamics the time dependent terms in (A.6a) will correspond to Lindblad resonances, while in (A.6b) they will correspond to vertical resonances. However the $k = 0$ terms in (A.6), which are *time independent* represent the potentials that are due to the perturber's *time-averaged* forcings. It is worth noting that if m' were smeared out into an inclined ring, the perturbing ring's potential would simply be $[\phi_0(r) + \phi_{z,0}(r, z)]/2$.

Since we are only interested in the global structure of our circumstellar dust-disk, we will ignore all the resonant terms in the above Fourier expansions. We can justify discarding these resonant terms since, as Chapter 4 notes, each resonance occupies a very narrow radial extent. Thus these resonances usually do not affect the global structure of a circumstellar dust-disk. So for our subsequent analysis we shall ignore all but the $k = 0$ terms in (A.6), which is equivalent to m experiencing the gravitational attraction from an inclined ring of material with mass m'.

To obtain the coefficients $\phi_k(r)$ and $\phi_{z,k}(r, z)$ we substitute (A.4) into (A.6), then multiply both sides by $\cos(k'\theta)$ and integrate over all θ:

$$-Gm' \int_{-\pi}^{\pi} \frac{\cos(k'\theta)}{\Delta_0} d\theta = \sum_{k=0}^{\infty} \frac{1}{1 + \delta_{k0}} \phi_k(r) \int_{-\pi}^{\pi} \cos[k(\theta - n't)] \cos(k'\theta) d\theta \tag{A.7a}$$

$$\frac{Gm'}{2} \int_{-\pi}^{\pi} \frac{(z - z')^2}{\Delta_0^3} \cos(k'\theta) d\theta = \sum_{k=0}^{\infty} \frac{1}{1 + \delta_{k0}} \phi_{z,k}(r, z) \int_{-\pi}^{\pi} \cos[k(\theta - n't)] \cos(k'\theta) d\theta \tag{A.7b}$$

where k' is and arbitrary integer and δ_{ij} is the Kronecker delta.

Utilizing the orthogonality relation for cosine:

$$\int_{-\pi}^{\pi} \cos(k'\theta) \cos(k\theta) d\theta = \pi(1 + \delta_{k0}) \delta_{kk'}$$

where the δ_{k0} accounts for the case when $k = k' = 0$.

The integrals on the right hand side of (A.7) can then be evaluated

$$-Gm' \int_{-\pi}^{\pi} \frac{\cos(k'\theta)}{\Delta_0} d\theta = \pi \sum_{k=0}^{\infty} \delta_{kk'} \phi_k(r) \cos(kn't) \tag{A.8a}$$

$$\frac{Gm'}{2} \int_{-\pi}^{\pi} \frac{(z-z')^2}{\Delta_0^3} \cos(k'\theta) d\theta = \pi \sum_{k=0}^{\infty} \delta_{kk'} \phi_{z,k}(r,z) \cos(kn't) \tag{A.8b}$$

Since $\delta_{kk'}$ is only non-zero when $k = k'$, then the sums in (A.8) reduce to a single term. Isolating $\phi_k(r)$ and $\phi_{z,k}(r,z)$ in (A.8) yields the desired Fourier amplitudes

$$\phi_k(r) = -\frac{Gm'}{\pi \cos(kn't)} \int_{-\pi}^{\pi} \frac{\cos(k\theta)}{\Delta_0} d\theta \tag{A.9a}$$

$$\phi_{z,k}(r,z) = \frac{Gm'}{2\pi \cos(kn't)} \int_{-\pi}^{\pi} \frac{(z-z')^2}{\Delta_0^3} \cos(k\theta) d\theta \tag{A.9b}$$

Since we are only interested in the $k = 0$ terms, this reduces to

$$\phi_0(r) = -\frac{Gm'}{\pi} \int_{-\pi}^{\pi} \frac{d\theta}{\Delta_0} \tag{A.10a}$$

$$\phi_{z,0}(r,z) = \frac{Gm'}{2\pi} \int_{-\pi}^{\pi} \frac{z^2 - 2zz' + z'^2}{\Delta_0^3} d\theta \tag{A.10b}$$

Since we can write $\Delta_0 = r'\sqrt{1 - 2\beta\cos(\theta - \theta') + \beta^2}$ with $\beta \equiv r/r'$, then

$$\phi_0(r) = -\frac{Gm'}{\pi r'} \int_{-\pi}^{\pi} \frac{d\theta}{\sqrt{1 - 2\beta\cos(\theta - \theta') + \beta^2}} \tag{A.11a}$$

$$\phi_{z,0}(r,z) = \frac{Gm'}{2\pi r'^3} \int_{-\pi}^{\pi} \frac{z^2 - 2zz'}{[1 - 2\beta\cos(\theta - \theta') + \beta^2]^{3/2}} d\theta \tag{A.11b}$$

where we have dropped the z'^2 term in (A.11b) since it does not contribute to the vertical acceleration $a_z = -\partial\Phi_z/\partial z$.

If we note that $z' \simeq r' \sin I' \sin(\theta' - \Omega')$ for circular, low inclination orbits (see Figure A.2) where Ω' is the longitude of ascending node which corresponds to the longitude where the orbit plane "ascends" through the $\hat{x}$-$\hat{y}$ reference plane. Thus

$$\phi_0(r) = -\frac{Gm'}{\pi r'} \int_{-\pi}^{\pi} \frac{d\psi}{\sqrt{1 - 2\beta\cos\psi + \beta^2}} \tag{A.12a}$$

$$\phi_{z,0}(r,z) = \frac{Gm'}{2\pi r'^3} \int_{-\pi}^{\pi} \frac{z^2 - 2zr' \sin I' \sin(\theta - \Omega' - \psi)}{(1 - 2\beta\cos\psi + \beta^2)^{3/2}} d\psi \tag{A.12b}$$

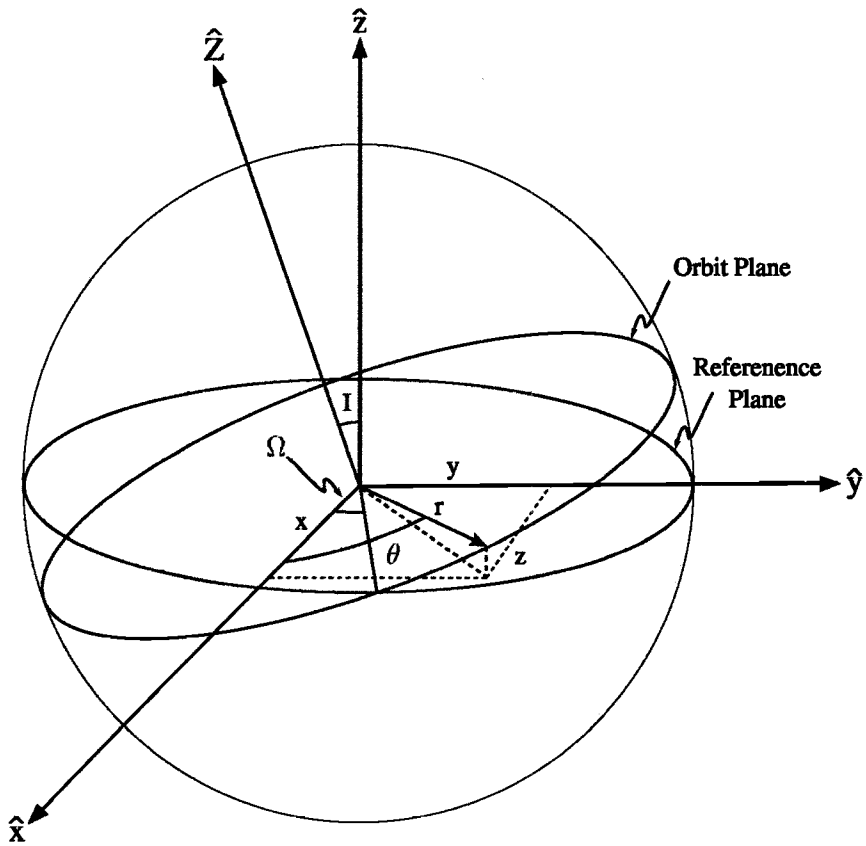

Figure A.2: For circular, low inclination orbits: $x \simeq r\cos\theta$, $y \simeq r\sin\theta$ and $z \simeq r\sin I\sin(\theta-\Omega)$.

where we have changed variables to $\psi = \theta - \theta'$.

We can simplify (A.12b) by utilizing the sine sum formula $\sin(\theta-\Omega'-\psi) - \cos\psi\sin(\theta-\Omega') - \sin\psi\cos(\theta-\Omega')$ and noting:

$$\int_{-\pi}^{\pi} \frac{\sin\psi d\psi}{(1-2\beta\cos\psi+\beta^2)^{3/2}} = 0$$

since the integrand is an odd function of ψ. Thus we can replace $\sin(\theta-\Omega'-\psi)$ with $\cos\psi\sin(\theta-\Omega')$ in (A.12b) since $\sin\psi\cos(\theta-\Omega')$ does not contribute to the integral.

Thus (A.12) can be written

$$\phi_0(r) = -\frac{Gm'}{\pi r'}\int_{-\pi}^{\pi} \frac{d\psi}{\sqrt{1-2\beta\cos\psi+\beta^2}} \tag{A.13a}$$

$$\phi_{z,0}(r,z) = \frac{Gm'}{2\pi r'^3}\int_{-\pi}^{\pi} \frac{z^2 - 2zr'\sin I'\sin(\theta-\Omega')\cos\psi}{(1-2\beta\cos\psi+\beta^2)^{3/2}} d\psi \tag{A.13b}$$

At this point we find it convenient to write the above in terms of Laplace coefficients:

$$b_s^{(j)}(\beta) \equiv \frac{1}{\pi}\int_{-\pi}^{\pi} \frac{\cos(j\psi)d\psi}{(1-2\beta\cos\psi+\beta^2)^s} \tag{A.14}$$

so

$$\Phi_0(r,\theta,t) \simeq -\frac{Gm'}{2r'} b_{1/2}^{(0)}(\beta) \tag{A.15a}$$

$$\Phi_z(r,\theta,z,t) \simeq \frac{Gm'}{4r'^3}[z^2 b_{3/2}^{(0)}(\beta) - 2zr'\sin I'\sin(\theta-\Omega')b_{3/2}^{(1)}(\beta)]. \tag{A.15b}$$

The secular accelerations (A.5) can be written using the chain rule

$$a_x = -\frac{\partial\Phi_0}{\partial\beta}\frac{\partial\beta}{\partial x} \tag{A.16a}$$

$$a_y = -\frac{\partial\Phi_0}{\partial y}\frac{\partial\beta}{\partial x} \tag{A.16b}$$

$$a_z = -\frac{\partial\Phi_z}{\partial z} \tag{A.16c}$$

where $\beta = r/r'$ with $r = \sqrt{x^2+y^2}$, so

$$\frac{\partial\beta}{\partial x} = \frac{x}{rr'} \tag{A.17a}$$

$$\frac{\partial\beta}{\partial x} = \frac{y}{rr'} \tag{A.17b}$$

Substituting (A.15) into (A.16) and using (A.17)

$$a_x = \frac{Gm'}{2r'^2}\frac{db_{1/2}^{(0)}(\beta)}{d\beta}\cos\theta \tag{A.18a}$$

$$a_y = \frac{Gm'}{2r'^2}\frac{db_{1/2}^{(0)}(\beta)}{d\beta}\sin\theta \tag{A.18b}$$

$$a_z = \frac{Gm'}{2r'^2}[\sin I'\sin(\theta-\Omega')b_{3/2}^{(1)}(\beta) - \beta\sin I\sin(\theta-\Omega)b_{3/2}^{(0)}(\beta)] \tag{A.18c}$$

where $x \simeq r\cos\theta$, $y \simeq r\sin\theta$ and $z \simeq r\sin I\sin(\theta-\Omega)$ to lowest-order in the small inclination I.

If we note the following the property of the Laplace coefficients

$$b_s^{(j)}(\beta^{-1}) = \frac{1}{\pi}\int_{-\pi}^{\pi}\frac{\beta^{2s}\cos(j\psi)d\psi}{(1-2\beta\cos\psi+\beta^2)^s} = \beta^{2s}b_s^{(j)}(\beta) \tag{A.19}$$

and if we define $\alpha \equiv \beta^{-1} = r'/r$, then we can write

$$a_x = \frac{Gm'}{2r^2}[\alpha b_{3/2}^{(1)}(\alpha) - b_{3/2}^{(0)}(\alpha)]\cos\theta \tag{A.20a}$$

$$a_y = \frac{Gm'}{2r^2}[\alpha b_{3/2}^{(1)}(\alpha) - b_{3/2}^{(0)}(\alpha)]\sin\theta \tag{A.20b}$$

$$a_z = \frac{Gm'}{2r^2}[\sin I' \sin(\theta - \Omega')b_{3/2}^{(1)}(\alpha) - \alpha \sin I \sin(\theta - \Omega)b_{3/2}^{(0)}(\alpha)] \tag{A.20c}$$

where the above also employed

$$\frac{db_{1/2}^{(0)}(\alpha)}{d\alpha} = b_{3/2}^{(1)}(\alpha) - \alpha b_{3/2}^{(0)}(\alpha),$$

which can be obtained by differentiating (A.14).

Eqns (A.20) thus provide the *secular* part of the acceleration that the perturbing particle m' exerts on particle m.

Appendix B

The Secular Equations of Motion

In the following section we derive the equations for the secular evolution of a particle of mass m due to the perturbation of a particle of mass m'. The secular evolution of a particle is a result of considering only the $k = 0$ terms in Eqn (A.6), which are independent of time. This is equivalent to *time-averaging* the equations of motion, which effectively smears the perturbing mass m' over a ring. To obtain the secular equations of motion for m, we consider the torque that m experiences due to a ring of mass m'.

First let us assume that m and a ring of mass m' are on circular, mutually inclined orbits. The torque on m due to the ring m' is given by:

$$\vec{T} = m(\vec{\imath} \times \vec{a}) \tag{B.1}$$

where $\vec{\imath}$ is m's position vector and $\vec{a}$ is the acceleration that m experiences due to m'. In Cartesian coordinates, the $\hat{x}$ and $\hat{y}$ components of $\vec{T}$ are:

$$T_x = m(ya_z - za_y) \tag{B.2a}$$

$$T_y = m(za_x - xa_z) \tag{B.2b}$$

where the Cartesian components of the acceleration that m experiences from a ring of mass m' are Eqn (A.20).

So T_x and T_y are

$$T_x = \frac{Gmm'}{2r}[\sin I' \sin(\theta - \Omega') - \sin I \sin(\theta - \Omega)]\alpha b^{(1)}_{3/2}(\alpha) \sin\theta \tag{B.3a}$$

$$T_y = \frac{Gmm'}{2r}[\sin I \sin(\theta - \Omega) - \sin I' \sin(\theta - \Omega')]\alpha b^{(1)}_{3/2}(\alpha) \cos\theta \tag{B.3b}$$

where we have made use of $x \simeq r\cos\theta$, $y \simeq r\sin\theta$ and $z \simeq r\sin I\sin\theta$ for circular, low inclination orbits. I and Ω are m's inclination and longitude of ascending node, while I' and Ω' are the orbital elements for the ring of mass m'. The $b_s^{(j)}(\alpha)$ are the Laplace coefficients (A.14) with $\alpha \equiv r'/r$, and θ is m's longitude (see Figure A.1).

Since we are only concerned with the evolution of our system over timescales much longer than a single orbital period, we calculate the time-averaged torques $\langle T_x\rangle$ and $\langle T_y\rangle$,

$$\langle T_x\rangle = \frac{Gmm'}{4r}[\sin I'\cos\Omega' - \sin I\cos\Omega]\alpha b_{3/2}^{(1)}(\alpha) \tag{B.4a}$$

$$\langle T_y\rangle = \frac{Gmm'}{4r}[\sin I'\sin\Omega' - \sin I\sin\Omega]\alpha b_{3/2}^{(1)}(\alpha) \tag{B.4b}$$

where the angled brackets denote a time-average of these quantities over a single orbit of m.

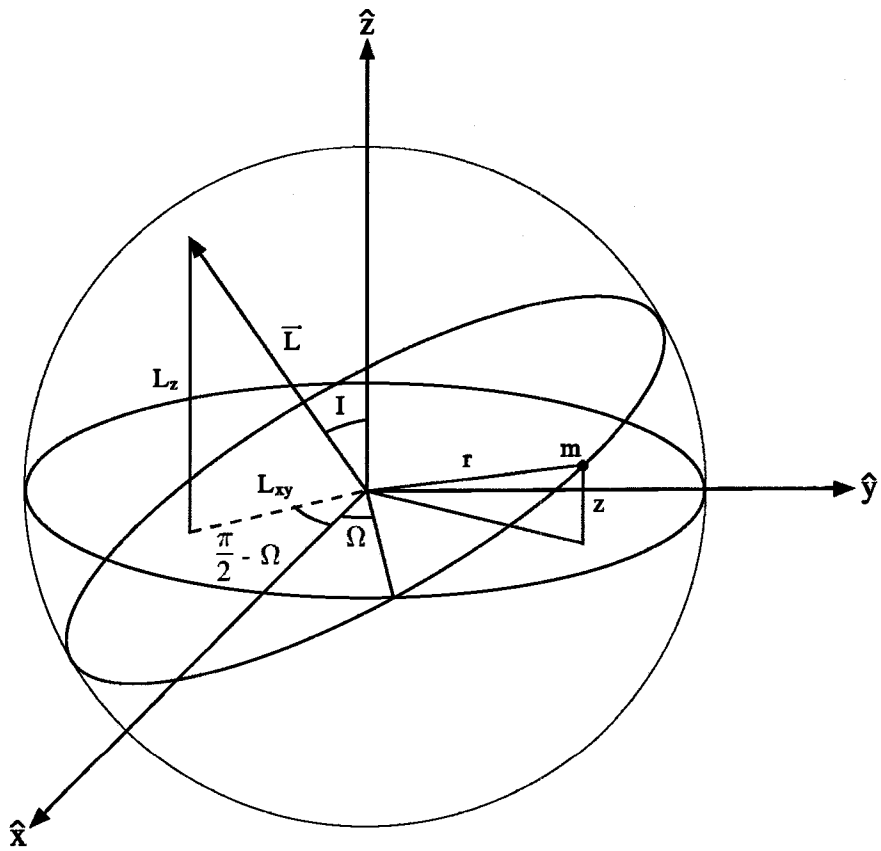

Figure B.1: Projections of the angular momentum vector

At this point we find it convenient to define two new quantities, p and q:

$$p \equiv \sin I \sin \Omega = \frac{L_x}{L} \tag{B.5a}$$

$$q \equiv \sin I \cos \Omega = -\frac{L_y}{L} \tag{B.5b}$$

with corresponding definitions for q' and p'; the p's and q's are the projections of a particle's angular momentum vector $\vec{L}$ onto the $\hat{x}$-$\hat{y}$ plane (see Figure B.1).

With the above definitions, we can write Eqn (B.4) in the more convenient form

$$\langle T_x \rangle = \frac{1}{4}\mu' m n^2 r^2 \alpha b_{3/2}^{(1)}(\alpha)(q' - q) \tag{B.6a}$$

$$\langle T_y \rangle = \frac{1}{4}\mu' m n^2 r^2 \alpha b_{3/2}^{(1)}(\alpha)(p' - p) \tag{B.6b}$$

where we have made use of $n^2 r^3 \equiv G(M_\star + m)$ with n being m's mean motion (*i.e.* average angular velocity), $\mu' \equiv m'/(M_\star + m) \ll 1$ is essentially the mass of the perturbing planet in units of the central star's mass $M_\star$.

Since the Cartesian components of m's angular momentum vector projected onto the $\hat{x}$-$\hat{y}$ plane are: $L_x = L \sin I \cos(\frac{\pi}{2} - \Omega) = L \sin I \sin \Omega$ and $L_y = -L \sin I \sin(\frac{\pi}{2} - \Omega) = -L \sin I \cos \Omega$, these can be written in terms of p and q:

$$L_x = pmna^2 \tag{B.7a}$$

$$L_y = -qmna^2 \tag{B.7b}$$

where we have made use of the magnitude of the angular momentum vector $|\vec{L}| \equiv mvr = mna^2$ for a body in a circular orbit.

Next differentiate the components of m's angular momentum in (B.7), and note that the rate of change of angular momentum is equal to the torque. If we time-average $\dot{L}_x$ and $\dot{L}_y$, we can equate them with the orbit averaged torques (B.6) and solve for $\langle \dot{p} \rangle$ and $\langle \dot{q} \rangle$:

$$\langle \dot{p} \rangle = \frac{1}{4}\mu' n \alpha b_{3/2}^{(1)}(\alpha)(q' - q) \tag{B.8a}$$

$$\langle \dot{q} \rangle = \frac{1}{4}\mu' n \alpha b_{3/2}^{(1)}(\alpha)(p - p') \tag{B.8b}$$

While the above solutions for $\langle \dot{p} \rangle$ and $\langle \dot{q} \rangle$ apply strictly to the case with two bodies (excluding the central star), it is simple to extend these results to the more general case with N bodies:

$$\langle \dot{p}_j \rangle = B_{jj} q_j + \sum_{\substack{j=1 \\ i \neq j}}^{N} B_{ji} q_i \tag{B.9a}$$

$$\langle \dot{q}_j \rangle = -B_{jj} p_j - \sum_{\substack{i=1 \\ i \neq j}}^{N} B_{ji} p_i \tag{B.9b}$$

where

$$B_{ji} = +\frac{1}{4} n_j \mu_{ji} \alpha_{ji} b^{(1)}_{3/2}(\alpha_{ji}) \qquad B_{jj} = -n_j \frac{1}{4} \sum_{\substack{i=1 \\ i \neq j}}^{N} \mu_{ji} \alpha_{ji} b^{(1)}_{3/2}(\alpha_{ji}) \tag{B.10a}$$

where n_j is the mean motion of m_j, $\alpha_{ji} \equiv a_i / a_j$ is the semi-major axis ratio between m_j and m_i, while $\mu_{ji} \equiv m_i / (M_\star + m_j)$ and $M_\star$ is the mass of the central star.

A similar derivation for the time-averaged equations of motion for the two other secularly varying orbital elements, $h = e \sin \varpi$ and $k = e \cos \varpi$, can be found in Murray & Dermott (1999), where the k and h are the x and y components of m's Laplace-Runge-Lenz vector, respectively. The Laplace-Runge-Lenz vector is constant for any motion generated by an inverse-squared force law (*i.e.* gravity and electrostatics). For brevity we shall omit the derivation here and simply quote the final results:

$$\langle \dot{h}_j \rangle = A_{jj} k_j + \sum_{\substack{i=1 \\ i \neq j}}^{N} A_{ji} k_i \tag{B.11a}$$

$$\langle \dot{k}_j \rangle = -A_{jj} h_j - \sum_{\substack{i-1 \\ i \neq j}}^{N} A_{ji} h_i \tag{B.11b}$$

where

$$A_{ji} = -\frac{1}{4} n_j \mu_{ji} \alpha_{ji} b^{(2)}_{3/2}(\alpha_{ji}) \qquad A_{jj} = +n_j \frac{1}{4} \sum_{\substack{i=1 \\ i \neq j}}^{N} \mu_{ji} \alpha_{ji} b^{(1)}_{3/2}(\alpha_{ji}) \tag{B.12a}$$

where the quantities A_{ji} and B_{ji} can be thought of as the constant elements of two $N \times N$ matrices $\mathbf{A}$ and $\mathbf{B}$ whose entries describe the magnitude of the mutual gravitational interactions that are exerted among the N planets (Murray & Dermott, 1999; Hahn, 2003).

Appendix C

The Lifetime of Circumstellar Dust

In the following section we look at the lifetime of dust grains in a circumstellar environment by comparing the collision timescale (t_{coll}) between dust grains, and the Poynting-Robertson (PR) drag timescale (t_{PR}). If $t_{coll} \gg t_{PR}$ the dust grains will spiral in towards the central star due to PR drag, but if $t_{coll} \ll t_{PR}$ then the dust grains will not drift very far before they get destroyed by a collision. In the derivation of secular perturbation theory in §4, it is tacitly assumed that bodies do not experience any significant radial drift, which requires that $t_{coll} \ll t_{PR}$.

C.1 Collision Timescale

We begin by considering a circumstellar disk occupied by dust grains, and a single dust grain on an inclined orbit with respect to the disk. To simplify matters, we shall assume that all the dust grains are on circular orbits and all have the same size. This is admittedly a crude approximation, since dust generally have a range of sizes, but this approximation is good enough for our order-of-magnitude assessment of collisions and PR drag.

If $\mathcal{P}_{coll}(r)$ is the probability per unit time that the dust grain will collide with another dust grain during its orbit, then we can write:

$$\mathcal{P}_{coll}(r) = \frac{2\tau(r)}{P_{orb}(r)} \tag{C.1}$$

where $\tau(r)$ is the dust-disk's normal optical depth that physically represents the fraction of the disk occupied by dust grains, with the factor of two accounting for the inclined dust grain penetrating the mid-plane of the disk twice per orbit.

A collision with another dust grain is certain to occur after a time t_{coll}, which satisfies

$$\mathcal{P}_{coll}(r)t_{coll}(r) = 1, \tag{C.2}$$

so

$$t_{coll}(r) = \frac{P_{orb}(r)}{2\tau(r)} \tag{C.3}$$

is the collision timescale.

It is worth noting that the above derivation of $t_{coll}(r)$ is by no means comprehensive, a more general treatment would need to take into account: the size distribution and the spatial distribution of the dust grains. Since the information on these distributions are largely unknown, incorporating them would only introduce more uncertainties. So for our proposes, the expression (C.3) provides an adequate estimate of the collision timescale. For completeness, the reader is directed toward a paper by Wyatt *et al.* (2002) for a more exhaustive analysis of collisional processes.

C.2 Poynting-Robertson Drag Timescale

Burns *et al.* (1979a) describes in detail the physics of radiation forces on small particles, and derived the acceleration of the grain's position vector $\vec{r}(t)$ due to radiation forces as the sum of two parts:

$$\ddot{\mathbf{r}} = \mathbf{a}_{rad} + \mathbf{a}_{PR} \tag{C.4}$$

where $\mathbf{a}_{rad} = a_{rad}\hat{r}$ is the acceleration due to radiation pressure, and

$$\mathbf{a}_{PR} = -a_{rad}\left(\frac{2\dot{r}}{c}\hat{r} + \frac{r\dot{\theta}}{c}\hat{\theta}\right) \tag{C.5}$$

is the acceleration due to PoyntingRobertson drag, where $a_{rad} = \beta GM_{\star}/r^2$ is the magnitude of the radiation pressure and $\beta \equiv F_{rad}/F_{grav}$ is the ratio of the radiation force to the gravitational force, and where $\dot{r}$ and $\dot{\theta}$ are the dust grain's radial and angular velocity, respectively. In the above, $\hat{r}$ and $\hat{\theta}$ are the radial and tangential unit vectors, and c is the speed of light.

The velocity independent term of the radiation force, $\mathbf{a}_{rad}$, is referred to as the radiation pressure, and it does not cause any radial drift. The quantity β is independent of r since F_{rad} and F_{grav} both

have the same radial dependence (*i.e.* both vary as r^{-2}). Though β is independent of r, it does have an inverse size dependence: $\beta = (0.5739 Q_{PR}/\rho s)(L_\star/L_\odot)(M_\odot/M_\star)$, where ρ is measured in g/cm^3 and s in μm (Burns *et al.*, 1979a). Q_{PR} is the radiation pressure efficiency factor which takes into account both the absorption and scattering efficiencies of a particle. In this study, we assume that $Q_{PR} = 1$ since a typical silicate grain of size $s \sim 10$ μm at optical wavelengths (*i.e.* $\lambda \sim 0.6$ μm) has a $Q_{PR} \sim 1$ (Wolf & Voshchinnikov, 2004). The inverse size dependence in the radiation force preferentially affects smaller, rather than larger dust grains.

The velocity dependent terms of the radiation force, Eqn (C.5), are collectively known as Poynting-Robertson (PR) drag. This component results in the loss of angular momentum from a particle's orbit[1], and causes the particle to spiral in toward the star. If we assume that a particle is initially in a circular orbit, it can then be shown that it will drift inwards with a radial velocity

$$\dot{r} = -2\alpha n r \tag{C.6}$$

where $\alpha \equiv \beta(nr/c) = 3.8\times10^{-5}(\mu\text{m}/s)(\text{g cm}^{-3}/\rho)(100\text{ AU}/r)^{1/2}$ is the dimensionless drag coefficient (Burns *et al.*, 1979a) evaluated at $r - 100$ AU for the β Pictoris system, which is the typical distance that is of interest here.

The orbit-decay timescale due to PR drag is defined through:

$$\int_r^0 r' dr' = -\frac{2GM_\star\beta}{c}\int_0^{t_{pr}(r)} dt \tag{C.7}$$

where we have substituted $\alpha = \beta(nr/c)$ and $n^2r^3 = GM_\star$ in Eqn (C.6).

This integrates to give

$$t_{pr}(r) = \frac{cr^2}{4GM_\star\beta} \tag{C.8}$$

and if we substitute for $GM_\star = n^2r^3$, $n = 2\pi/P_{orb}$ and write Eqn (C.8) in terms of α, then

$$t_{PR}(r) = \frac{P_{orb}(r)}{8\pi\alpha} \tag{C.9}$$

where $P_{orb}(r)$ is the the mean orbital period at a distance r from the star.

[1]That angular momentum is carried away by stellar photons that are scattered by the dust grain.

C.3 Comparison of Collision and PR Timescales

At this point, we make a comparison of the collision and PR timescales as derived in the previous two sections. As mentioned, the application of secular perturbation theory stipulates that the particles do not experience any radial drift. This requires $t_{coll}(r) \ll t_{PR}(r)$ which requires the disk's optical depth to be sufficiently high, *i.e.*

$$\tau(r) \gg \tau_{crit}(r) \equiv 4\pi\alpha \tag{C.10}$$

where $\tau_{crit}(r)$ is the optical depth when $t_{coll}(r) = t_{PR}(r)$.

Before we can proceed, we need the typical dust grain size at β Pictoris. We expect a dust grain density of $\rho \sim 2.0$ g/cm^3, which is typical of silicate dust grains. The dust grain size can be inferred from the neutral optical colours of the circumstellar disk around β Pictoris, which implies that the dust grains are much larger than optical wavelength photons (*i.e.* $s \gg \lambda \sim 0.6$ μm). Theoretical models and observational evidence for β Pictoris indicate that a typical dust grain size is $s \simeq 10.0$ μm (Krivov *et al.*, 2000). Utilizing these fiducial values for the dust grain size and density gives: $\tau_{crit}(r) = 2.4 \times 10^{-5}(100 \text{ AU}/r)^{1/2}$.

Artymowicz was able to determine the functional form of the normal optical depth by inverting the scattered-light images of β Pictoris (Artymowicz *et al.*, 1989; Artymowicz, 1997), who reports $\tau(r) = 4.8 \times 10^{-3}$ at $r = 100$ AU which gives $\tau(r)/\tau_{crit}(r) \simeq 200$. This implies that $t_{coll}(r) \ll t_{PR}(r)$, thus we can conclude that the circumstellar disk around β Pictoris is a collisionally dominated disk, and we can safely apply secular perturbation theory to this system.

Appendix D

The Inclination Distribution

In this appendix we derive the form of the inclination distribution utilized in **ringworld**. The relationship between the projected latitude distribution $h(r,\theta)$ and its corresponding inclination distribution $H(r,I)$ is given by Brown (2001):

$$h(r,\theta) = \int_{\theta}^{\pi/2} \frac{H(r,I)dI}{\sqrt{\sin I^2 - \sin\theta^2}} \tag{D.1}$$

where we note that an isotropic distribution of particles has an inclination distribution $H(r,I) = (2/\pi)\sin I$, which results in a latitude distribution $h(r,\theta) = 1$.

In general, Eqn (D.1) is a Volterra integral equation of the first kind:

$$f(x) = \int_{x}^{a} \frac{y(t)dt}{\sqrt{g(x)^2 - g(t)^2}} \tag{D.2}$$

which has the solution (Polyanin & Manzhirov, 1998)

$$y(x) = \frac{1}{\pi}\frac{d}{dx}\int_{x}^{a} \frac{f(t)g'(t)dt}{\sqrt{g(x)^2 - g(t)^2}} \tag{D.3}$$

where it is assumed that $g'(t) > 0$.

Thus the solution to Eqn (D.1) is given by

$$H(r,I) = \frac{\partial G(r,I)}{\partial I} \tag{D.4}$$

where

$$G(r,I) = -\frac{2}{\pi}\int_{I}^{\pi/2} \frac{h(r,\theta)\sin\theta\cos\theta d\theta}{\sqrt{\sin\theta^2 - \sin I^2}} \tag{D.5}$$

We now turn our attention to the projected vertical distribution from Artymowicz *et al.* (1989):

$$h(r,z) - \exp\left\{-\left[\frac{z}{\zeta(r)}\right]^{\gamma}\right\} \tag{D.6}$$

where γ controls the latitude distribution of the dust (*e.g.* $\gamma = 1$ for an exponential distribution and $\gamma = 2$ for a Gaussian distribution) and $\zeta(r)$ is the vertical scale height

$$\zeta(r) = \zeta_0 \left(\frac{r}{r_0}\right)^{\delta'} \tag{D.7}$$

where δ' controls the flaring of the disk, and ζ_0 is the vertical thickness of the disk at $r = r_0$.

Transforming Eqn (D.6) to a projected latitude distribution we replace $z = r\sin\theta \simeq r\theta$ in the small angle approximation

$$h(r,\theta) = \exp\left\{-\left[\frac{\theta}{w(r)}\right]^{\gamma}\right\} \tag{D.8}$$

and $w(r)$ is the latitudinal scale height

$$w(r) = w_0 \left(\frac{r}{r_0}\right)^{\delta} \tag{D.9}$$

where $\delta = \delta' - 1$ and $w_0 = \zeta_0/r_0$.

Unfortunately, Eqn (D.4) is not easily solvable for the latitude distribution (D.8), due to the singular nature of the integrand as θ approaches I. However, if we assume that the dominant contribution to the integral will occur when $\theta \simeq I$ we can replace $\mathbf{e}^{-[\theta/w(r)]^{\gamma}} \rightarrow \mathbf{e}^{-[I/w(r)]^{\gamma}}$, so

$$G(r,I) \simeq -\frac{2}{\pi}\mathbf{e}^{-[I/w(r)]^{\gamma}} \int_I^{\pi/2} \frac{\sin\theta\cos\theta d\theta}{\sqrt{\sin\theta^2 - \sin I^2}} = -\frac{2}{\pi}\mathbf{e}^{-[I/w(r)]^{\gamma}}\cos I \tag{D.10}$$

As long as $w(r) \ll 1$, then we can assume that $\cos I \simeq 1$ and $G(r,I) \simeq -(2/\pi)\mathbf{e}^{-[I/w(r)]^{\gamma}}$, which gives the inclination distribution

$$H(r,I) \simeq \frac{2}{\pi w(r)}\left(\frac{I}{w(r)}\right)^{\gamma-1}\mathbf{e}^{-[I/w(r)]^{\gamma}} \tag{D.11}$$

To make use of this inclination distribution in our Monte Carlo image generation, we utilize the procedure outlined in §5.1 and we find:

$$I_p(r,\xi) \simeq w(r)[-\ln[1+\xi(\mathbf{e}^{-[2/\pi w(r)]^{\gamma}} - 1)]]^{1/\gamma} \tag{D.12}$$

where ξ is a random number uniformly distributed over $(0,1)$.

However, if $w(r) \ll 1$, then $e^{-|2/\pi w(r)|^\gamma} \simeq 0$ and we finally arrive at the generating function for the proper inclination distribution used in **ringworld**:

$$I_p(r, \xi) \simeq w(r)[-\ln(\xi)]^{1/\gamma} \tag{D.13}$$

Bibliography

Alibert, Y., Mordasini, C., Benz, W., & Winisdoerffer, C. 2005, A & A, **434**, 343

Andrews, S. M., Williams, J. P. 2005, ApJ, **631**, 1134

Artymowicz, P. 1988, ApJ, **335**, L79

Artymowicz, P., Burrows, C. J., & Paresce, F. 1989, ApJ, **337**, 494

Artymowicz, P., Paresce, F., & Burrows, C. J. 1990, Adv. Space Res., **10**, (3)81

Artymowicz, P. 1997, Ann. Rev. Earth Planet Sci., **25**, 175

Artymowicz, P., Clampin, M. 1997, ApJ, **490**, 863

Augureau, J. C., Nelson, R. P., Lagrange, A. M., Papaloizou, J. C. B., & Mouillet, D. 2001, A & A, **370**, 447

Aumann, H. H. 1985, PASP, **97**, 885

Barrado y Navascués, D., Stauffer, J. R., Song, I., Caillault, J.-P. 1999, ApJ, **520**, 123

Beckwith, S. V. W. 1999, *The Origin of Stars and Planetary Systems* (Kluwer Academic Publishers, eds Charles J. Lada & Nikolaos D. Kylafis), p. 579

Beust, H., Vidal-Madjar, A., Lagrange-Henri, A. M., & Ferlet, R. 1990, A & A, **236**, 202

Beust, H., & Morbidelli, A. 1996, Icarus, **120**, 358

Boyce, W., DiPrima, R. 1997, *Elementary Differential Equations and Boundary Value Problems*, Sixth Edition (John Wiley Sons Inc.), p. 370

Brandeker, A., Liseau, R. G. & Fridlund, M. 2004, A & A, **413**, 681

Brouwer, D., Clemence, G. M. 1961, *Methods of Celestial Mechanics* (New York: Academic Press)

Brown, M. E. 2001, AJ, **121**, 2804

Burns, J. A., Lamy, P. L., Soter, S. 1979, Icarus, **40**, 1B

Burns, J. A., Cuzzi, J. N., Durisen, R. H., Hamill, P. 1979, AJ, **84**, 1783

Charbonneau, P. 1995, ApJS, **101**, 309

Crifo, F., Vidal-Madjar, A., Lallement, R., Ferlet, R., & Gerbaldi, M. 1997, A & A, **320**, L29

Danby, J. M. A. 1992, *Fundamentals of Celestial Mechanics* (Richmond, Virginia: Willmann-Bell Inc.)

Dent, W. R. F., Walker, H. J., W. S. Holland, W. S. & Greaves, J. S. 2000, MNRAS, **314**, 702

Dermott, S. F. & Nicholson, P. D. 1989, *Higlights of Astronomy*, **8**, 259

Di Folco, E., Thévenin, F., Kervella, P., Domiciano de Souza, A., Coudé du Foresto, V., Ségransan, D., & P. Morel, P. 2004, A & A, **426**, 601

Dohnanyi, J. W. 1969, J. Geophys. Res., **74**, 2531

Gledhill, T. M., Scarrott, S. M., & Wolstencroft, R. D. 1991, MNRAS, **252**, 50

Grady, C. A., Sitko, M. L., Russell, R. W., Lynch, D. K., Hanner, M. S., Perez, M. R., Bjorkman, K. S.; de Winter, D. 2000, *Protostars and Planets IV* (Tucson: University of Arizona Press; eds Mannings, V., Boss, A. P., & Russell, S. S.), p.613

Goldreich, P., Ward, W. R. 1973, ApJ, **183**, 1051

Golimowski, D. A., Ardila, D. R., Krist, J. E., Clampin, M., Ford, H. C., Illingworth, G. D., Bartko, F., Benítez, N., Blakeslee, J. P., Bouwens, R. J., Bradley, L. D., Broadhurst, T. J., Brown, R. A.,

Burrows, C. J., Cheng, E. S., Cross, N. J. G., Demarco, R., Feldman, P. D., Franx, M., Goto, T., Gronwall, C., Hartig, G. F., Holden, B. P., Homeier, N. L., Infante, L., Jee, M. J., Kimble, R. A., Lesser, M. P., Martel, A. R., Mei, S., Menanteau, F., Tsvetanov, Z. I., White, R. L., Zheng, W. & Zirm, A. W. 2006, AJ, **131**, 3109

Hahn, J. M. 2003, ApJ, **595**, 531

Hayashi, C. 1981, Prog. Theor. Phys. Suppl., **70**, 35

Heap, S. R., Lindler, D. J., Lanz, T. M., Cornett, R. H., Hubeny, I., Maran, S. P., & Woodgate, B. 2000, ApJ, **539**, 435

Henyey, L. G, & Greenstein, J. L. 1941, ApJ, **93**, 70

Hoffleit, D. and Warren, W.H. Jr., *The Bright Star Catalogue*, 5th Revised Edition, Version 2, 1994

Hollenbach, D. J., Yorke, H. W., Johnstone, D. 2000, *Protostars and Planets IV* (Tucson: University of Arizona Press; eds Mannings, V., Boss, A. P., & Russell, S. S.), p. 401

Hong, S. S. 1985, A & A, **146**, 67

Kalas, P., & Jewitt, D. 1995, AJ, **110**, 794

Kalas, P., Larwood, J., Smith, B. A., & Schultz, A. 2000, ApJ, **530**, L133

Kalas, P., Graham. J. R. & Clampin, M. C. 2005, *Nature*, **435**, 1067

Knacke, R. F., Fajardo-Acosta, S. B., Telesco, C. M., Hackwell, J. A., Lynch, D. K., Russell, R. W. 1993, ApJ, **418**, 440

Krivov, A. V., Mann, I. & Krivova, N. A. 2000, A & A, **362**, 1127

Krivova, N. A., Krivov, A. V., & Mann, I. 2000, ApJ, **539**, 424

Lagrange-Henri, A. M., Vidal-Madjar, A., Ferlet, R. 1988, A & A, **190**, 275

Lagrange-Henri, A. M., Beust, H., Mouillet, D., Deleuil, M., Feldman, P. D., Ferlet, R., Hobbs, L., Lecavelier des Etangs, A., Lissauer, J. J., McGrath, M. A., McPhate, J. B., Spyromilio, J., Tobin, W., & Vidal-Madjar, A. 1998, A & A, **330**, 1091

Larwood, J. D., & Kalas, P. G. 2001, MNRAS, **323**, 402

Lanz, T., Heap, S. R., & Hubeny, I. 1995, ApJL, **447**, 41

Lecavelier des Etangs, A., *et al.*1993, A & A, **274**, 877

Lecavelier des Etangs, A., Vidal-Madjar, A., & Ferlet, R. 1996, A & A, **307**, 542

Lecavelier des Etangs, A., 2000, ASPC, **219**, 308

Levison, H. F., Duncan, M. J., Wetherill, G. W. 1994, *Nature*, **372**, 441

Li, A., & Greenberg, J. M. 1998, A & A, **331**, 291

Mouillet, D., Lagrange, A.-M., Beuzit, J.-L., & Renaud, N. 1997a, A & A, **324**, 1083

Mouillet, D., Larwood, J. D., Papaloizou, J. C. B., & Lagrange, A. M. 1997b, MNRAS, **292**, 896

Murray, C. D., & Dermott, S. F. 1999, *Solar System Dynamics* (New York: Cambridge University Press)

Nelder, J. A. & Mead, R. 1965, Comput. J., **7**, 308

Novotny, S. J., Ph.D. Thesis, University of Florida

Okamoto, Y. K., Kataza, H., Honda, M., Yamashita, T., Onaka, T., Watanabe, J. -I., Miyata, T., Sako, S., Fujiyoshi, T. & Sakon, I. 2004, *Nature*, **431**, 660

Olofsson, G., Liseau, R., & Brandeker, A. 2001, ApJ, **563**, 77

Patin, E., Lagage, P. O., Artymowicz, P. 1997, A & A, **327**, 1123

Paresce, F., & Burrows, C. 1987, ApJ, **319**, L23

Polyanin, A. D., Manzhirov, A. V. 1998, *Handbook of Integral Equations* (Boca Raton: CRC Press)

Press, W. H., Teukolsky, S. A., Vetterling, W. T., & Flannery, B. P. 1992, *Numerical Recipes in C: The Art of Scientific Computing*, Second Edition (Cambridge: Cambridge University Press)

Quillen, A. C., Thorndike, S. 2002, ApJ, **578L**, 149

Roberge, A., Feldman, P. D., Lagrange, A. M., Vidal-Madjar, A., Ferlet, R., Jolly, A., Lemaire, J. L., Rostas, F. 2000, ApJ, **538**, 904

Schneider, G., Smith, B. A., Becklin, E. E., Koerner, D. W., Meier, R., Hines, D. C., Lowrance, P. J., Terrile, R. J., Thompson, R. I., Rieke, M. 1999, ApJ, **513**, 127

Shu, F. H., Adams, F. C., Lizano, S. 1987, ARA & A, **25**, 23

Smith, B. A., & Terrile, R. J. 1984, Science, **226**, 1421

Strom, S. E., Edwards, S., Skrutskie, M. F. 1993, *Protostars and Planets III* (Tucson: University of Arizona Press; eds Levy, E. H. & Lunine, J. I.), pp. 837-866

Taylor, J. R. 1972, *Scattering Theory* (New York: Wiley)

Telesco, C. M. & Knacke, R. F. 1991, ApJ, **372**, 29

Telesco, C. M., Fisher, R. S., Wyatt, M. C., Dermott, S. F., Kehoe, T. J. J., Novotny, S., Mariñas, N., Radomski, J. T., Packham, C., De Buizer, J. & Hayward, T. L. 2005, *Nature*, **433**, 133

Thébault, P., Augereau, J. C., & Beust, H. 2003, A & A, **408**, 775

Thébault, P., Augereau, J. C. 2005, A & A, **437**, 141

Vidal-Madjar, A., Ferlet, R., Hobbs, L. M., Gry, C., & Albert, C. E. 1986, A & A, **167**, 325

Wahhaj, Z., Koerner, D. W., Ressler, M. E., Werner, M. W., Backman, D. E., & Sargent, A. I. 2003, ApJ, **584**, L27

Walmsley, C. M., Flower, D. R., Pineau des Forêts, G. 2004, A & A, **418**, 1035

Weidenschilling, S. J. 1980, Icarus, **44**, 172

Weinberger, A. J., Becklin, E. E., Zuckerman, B. 2003, ApJ, **584**, L33

Wisdom, J. 1980, AJ, **85**, 1122

Wolf, S., Voshchinnikov, N. V. 2004, Comput. Phys. Commun. **162**, 113

Wolstencroft, R. D., Scarrott, S. M., & Gledhill, T. M. 1995, AP & SS, **224**, 395

Wyatt, M. C., Dermott, S. F., Telesco, M., Fisher, R. S., Grogan, K., Holmes, E. K., & Piña, R. K. 1999, ApJ, **527**, 918

Wyatt, M. C., Dent, W. R. F. 2002, MNRAS, **334**, 589

Xu, Y. L., Dermott, S., Gustafson, B., Liou, J. 1993, LPICo, **810**, 317

Zuckerman, B. & Becklin, E. E. 1993, ApJ, **414**, 793